

SMA OBSERVATIONS OF THE EXTENDED $^{12}\text{CO}(J=6-5)$ EMISSION IN THE STARBURST GALAXY NGC 253

M. KRIPS¹, S. MARTÍN^{1,2}, A. B. PECK³, K. SAKAMOTO⁴, R. NERI¹, M. GURWELL⁵, G. PETITPAS⁵, AND JUN-HUI ZHAO⁵
Not to appear in Nonlearned J., 45.

ABSTRACT

We present observations of the $^{12}\text{CO}(J=6-5)$ line and 686 GHz continuum emission in NGC 253 with the Submillimeter Array at an angular resolution of $\sim 4''$. The $^{12}\text{CO}(J=6-5)$ emission is clearly detected along the disk and follows the distribution of the lower ^{12}CO line transitions with little variations of the line ratios. A large-velocity gradient analysis suggests a two-temperature model of the molecular gas in the disk, likely dominated by a combination of low-velocity shocks and the disk wide PDRs. Only marginal $^{12}\text{CO}(J=6-5)$ emission is detected in the vicinity of the expanding shells at the eastern and western edges of the disk. While the eastern shell contains gas even warmer ($T_{\text{kin}} > 300$ K) than the hot gas component ($T_{\text{kin}} = 300$ K) of the disk, the western shell is surrounded by gas much cooler ($T_{\text{kin}} = 60$ K) than the eastern shell but somewhat hotter than the cold gas component of the disk (for similar H_2 and CO column densities), indicative of different (or differently efficient) heating mechanisms. The continuum emission at 686 GHz in the disk agrees well in shape and size with that at lower (sub-)millimeter frequencies, exhibiting a spectral index consistent with thermal dust emission. We find dust temperatures of ~ 10 -30 K and largely optically thin emission. However, our fits suggest a second (more optically thick) dust component at higher temperatures ($T_{\text{d}} > 60$ K), similar to the molecular gas. We estimate a global dust mass of $\sim 10^6 M_{\odot}$ for the disk translating into a gas-to-dust mass ratio of a few hundred consistent with other nearby active galaxies.

Subject headings: galaxies: individual(NGC 253) – Galaxies: active – galaxies: ISM – galaxies: starburst – submillimeter: galaxies – galaxies: emission lines

1. INTRODUCTION

Submillimeter interferometric observations at frequencies above 400 GHz are technically difficult and rely on very dry atmospheric conditions. The reduced transmissivity of the atmosphere at submm wavelengths necessitates observing from a vantage point at high elevation ($\gtrsim 4000$ m above sea level). Before the advent of the Atacama Large Millimeter Array (ALMA), the only interferometer in the world offering the capability of observations at frequencies above 400 GHz was the Submillimeter Array (SMA) located at 4000 m altitude on Mauna Kea in Hawaii, USA. Equipped with 8 antennas of 6 m diameter and 690 GHz receivers, the SMA provides a window on warm and hot molecular gas and dust through the $^{12}\text{CO}(J=6-5)$ line and submillimeter continuum emission with high angular resolution. The analysis of spatially resolved warm molecular gas provides essential information to understand the complexity of the excitation conditions, chemistry and dynamics of the molecular gas in various environments, including star-forming regions, active galactic nuclei (AGN) and quiescent regions (e.g., Aladro et al. 2011; Krips et al. 2011, 2008; Martín et al. 2006). Moreover, given the explosion of detections of molecular gas at high redshifts

in the past decade, mostly through high rotational levels of CO, it is essential to have a robust understanding of the physics behind the CO ladder as a function of the energetic environments in which they are detected (e.g., Rosenberg et al. 2014; Papadopoulos et al. 2010, 2007; Weiß et al. 2005; Carilli et al. 2002). To date, only a handful of journal publications exist based on 690 GHz interferometric observations, most of which study galactic sources (e.g. Zapata et al. 2013; Rolffs et al. 2011; Matsushita et al. 2009; Nakashima et al. 2007; Qi et al. 2006; Beuther et al. 2006). Matsushita et al. (2009) present the first 690 GHz interferometric study of $^{12}\text{CO}(J=6-5)$ emission in a nearby extragalactic source, the ultra-luminous infrared galaxy Arp 220. Since then, mostly thanks to ALMA but also the SMA, a couple of interferometric observations of the $^{12}\text{CO}(J=6-5)$ emission in nearby galaxies have been very recently published (e.g., García-Burillo et al. 2014; Xu et al. 2014; Sliwa et al. 2013). In this paper, we present the first mosaic observations at 690 GHz of the nearby starburst galaxy NGC 253, made using the SMA.

NGC 253 is one of the best studied nearby (~ 3.5 Mpc, where $1'' = 17$ pc; Rekola et al. 2005; Mouhcine et al. 2005) infrared bright starburst galaxies ($3 \times 10^{10} L_{\odot}$; Tesco & Harper 1980). It is thus an ideal prototype to study the effects of a central starburst ($\sim 2-4 M_{\odot} \text{ yr}^{-1}$; Minh et al. 2007; Ott et al. 2005; Bendo et al. 2015) on the dynamics (NGC 253 is an edge-on galaxy), excitation conditions and chemistry of the surrounding molecular gas (e.g., Leroy et al. 2015; Meier et al. 2015; Bolatto et al. 2013; Sakamoto et al. 2011, 2006; Knudsen et al. 2007; Martín et al. 2006; Bradford et al. 2003). As a consequence of the starburst in the center of NGC 253, a high rate of supernova explosions

¹ Institut de RadioAstronomie Millimétrique, 300 rue de la Piscine, Domaine Universitaire, 38406 Saint Martin d'Hères, France; krips,smartin,neri@iram.fr

² European Southern Observatory, Avda Alonso de Córdova 3107, Vitacura, Santiago, Chile

³ National Radio Astronomy Observatory, 520 Edgemont Rd, Charlottesville, VA 22903, USA; apeck@nrao.edu

⁴ Academia Sinica, Institute of Astronomy and Astrophysics, Taiwan; ksakamoto@asiaa.sinica.edu.tw

⁵ Harvard-Smithsonian Center for Astrophysics, Cambridge, MA 02138; mgurwell,gpetitpa,jzhao@cfa.harvard.edu

TABLE 1
 OBSERVATION LOG

Line	Frequency (GHz)	Date (mm/yyyy)	rms ^a (mJy)	Δv (km s ⁻¹)	Beam ^b ("×")	Type ^c	Ref ^d
¹² CO(J=6-5)	691.473 (USB)	09/2007	7000	12	4''2×2''1	M	(1)
¹² CO(J=3-2) ^e	345.796 (LSB)	09/2007	100	12	5''8×4''5	M	(1)
¹² CO(J=3-2) ^e	345.796 (LSB)	09/2004	130	12	3''9×1''9	M	(2)
¹² CO(J=2-1) ^f	230.538 (LSB,USB)	2003-2005	30	12	1''7×1''5	SF	(2)
¹² CO(J=1-0)	115.271 (USB)	2011	4	12	3''7×2''7	M	(3)

^a The noise given here corresponds to the thermal noise, as derived from the visibility weights, i.e., system temperatures. The noise is given per individual mosaic field (see text for some more discussion).

^b “Original” synthesized resolution for natural weighting. Please note that all maps presented in this paper were brought to the same resolution of 4''2×2''1 using a uv-taper to change the weighting for the different baselines.

^c M=Mosaic; SF= Single Field

^d (1) this work; (2) Sakamoto et al. (2011); (3) ALMA science archive; project id: 2011.0.00172.S.

^e These two data sets were eventually combined (see text).

^f These data were taken using all available configurations of the SMA, with baselines ranging from 8 to 509m, as well observed in different sidebands.

(<0.2 yr⁻¹) has been observed (see Rampadarath et al. 2014; Paglione & Abrahams 2012). These are most likely responsible for a kiloparsec-scale outflow perpendicular to the disk (e.g., Fabbiano & Trinchierie 1984; Heckman et al. 1990). In addition to this outflow, Sakamoto et al. (2006) report on at least two expanding shells, or superbubbles, at the edges of the disk (named SB1 for the south-western shell and SB2 for the north-eastern one) that might be either caused by winds from and/or supernovae in a super star cluster or a hypernova(e); the possibility of a third shell, a bit more southern to SB2, was discussed as well. The authors further find a strongly disturbed molecular gas disk associated with young stellar clusters and stellar explosions as well as the large-scale super-wind. Their follow-up observations at ~1'' resolutions confirmed the SB2 (and the third shell) but SB1 was reported to be more complicated than appeared in previous lower-resolution data (Sakamoto et al. 2011). They noted that it may be a shell in a complicated shape or other gas kinematical feature that looks like a shell at low resolution. With very recent ALMA observations of ¹²CO(J=1-0) at 3'' resolution Bolatto et al. (2013) reported four shells in the central kpc of NGC 253. One is SB2 and three are clustered in/around the region of SB1. While SB2 can be connected to a compact stellar cluster, SB1 is found at the position of a compact radio continuum source that is associated with a supernova remnant (see Sakamoto et al. 2006; Bolatto et al. 2013). The nature of shells 2 and 4 remain unclear at this point, whether they are separate bubbles or connected to the stellar winds or other dynamical features.

A 2 mm line survey of NGC 253 done by Martín et al. (2006) reveals an impressive chemical richness and complexity in its center (see also Meier et al. 2015). NGC253 appears to resemble SgrB2, the region of molecular cloud complexes in the Galactic center, more than the evolved starburst galaxy M82 (see also Aladro et al. 2011) despite the fact that our Milky Way is not a starburst galaxy at all. Moreover, Sakamoto et al. (2011) find a striking resemblance between the molecular gas distribution of the Milky Way and that of NGC 253. The chemistry of the molecular gas in the central kpc of NGC 253 appears to be dominated by large-scale, low veloc-

ity shocks (e.g., Martín et al. 2006; García-Burillo et al. 2000). However, Martín et al. (2009) detect significant amounts of molecular tracers for photodissociation regions (PDRs) suggesting PDR chemistry also plays a significant role in this starburst galaxy. This is further supported by Rosenberg et al. (2012) and Rosenberg et al. (2014). The NIR H₂ emission appears to be mostly fluorescently excited favoring PDRs as the dominant excitation mechanism in the nuclear region of NGC 253. The only exceptions seem to be three small isolated regions in which shocks may play the leading role. Rosenberg et al. (2012) estimate that at most 30% of the H₂ emission is excited by shocks. Based on a ¹²CO and ¹³CO ladder analysis from Herschel and ground-based single-dish observations with a (normalised) beam of 32.5'', Rosenberg et al. (2014) present even more evidence for the combined contribution of PDR and mechanical heating of the molecular gas in the central disk of NGC 253. They also argue that heating by cosmic rays can be mostly neglected; at most a few percent could be attributed to cosmic ray heating in their models.

The paper is organised as follows: The observations and the archival data are discussed in Section 2. The results are discussed in Section 3 and a summary is given in Section 4.

2. OBSERVATIONS

First, we will present some general information on the SMA observations conducted for this paper. We will then briefly discuss previous ¹²CO(J=3-2) SMA observations that were eventually used to merge with the ¹²CO(J=3-2) observations carried out simultaneously with ¹²CO(J=6-5). We will give additional information on previous ¹²CO(J=2-1) SMA observations. These observations were taken from Sakamoto et al. (2011) and Sakamoto et al. (2006). New ¹²CO(J=1-0) ALMA observations of NGC 253 are also included in this study and are hence briefly presented as well. We will address the problem of missing short spacings and the significance of spatial filtering to our observations in Section 2.4. All data presented in this paper stem from mosaic observations (except the ¹²CO(J=2-1) data) and have hence been corrected for the respective primary beams.

TABLE 2
GENERAL RESULTS

Line ^{12}CO	$S_\nu^{\text{max,a}}$ (Jy)	$v_0^{\text{max,a}}$ (km s $^{-1}$)	$\text{FWHM}^{\text{max,a}}$ (km s $^{-1}$)	$\int (S_\nu dv)^{\text{b}}$ (Jy km s $^{-1}$)
J=6-5	350 \pm 15	0 \pm 3	130 \pm 7	(58 \pm 3) \times 10 3
J=3-2	347 \pm 3	0 \pm 1	140 \pm 7	(75 \pm 2) \times 10 3
J=2-1	111 \pm 2	0 \pm 1	167 \pm 8	(29 \pm 0.3) \times 10 3
J=1-0	30 \pm 1	0 \pm 1	165 \pm 8	(7.8 \pm 0.1) \times 10 3
Cont.	S_ν^{b} (Jy)			
ν_{obs}				
686 GHz	32 \pm 1.4			
350 GHz	2.6 \pm 0.1			
220 GHz	0.67 \pm 0.05			
115 GHz	0.26 \pm 0.01			

^a Peak fluxes, zero velocities and FWHM are given for the dominant maximum component of the multiple Gaussian fit. The zero velocity is with respect to the redshifted frequency of the respective CO line. The redshift of NGC 253 is $z=0.000811$ (see Koribalski et al. 2004)

^b Emission taken over the entire emission area covered with the 5-point mosaic by using a multiple Gaussian fit (up to 3 Gaussian lines are fitted).

2.1. SMA observations of $^{12}\text{CO}(J=6-5)$ and $^{12}\text{CO}(J=3-2)$

NGC 253 was observed using two receivers simultaneously to obtain $^{12}\text{CO}(J=6-5)$, $^{12}\text{CO}(J=3-2)$ and $\text{HCO}^+(J=4-3)$ ⁶ with the SMA. At the time of the observations, five of the eight SMA antennas were equipped with working 690 GHz receivers. All five antennas were placed in the inner ring of the array, known as the subcompact configuration, with baselines ranging from a few (~ 8 meters) up to 25 meters to allow for a good (u, v) coverage and reasonable angular resolution at 690 GHz. To cover most of the CO emission in NGC 253, a five-field mosaic (size $\sim 50''$) along the plane of the disk was observed with a spacing of half the primary beam size ($\sim 7.5''$) at 690 GHz between the pointing centers. The phase reference center of the central pointing was set to $\alpha(J2000)=00^{\text{h}}47^{\text{m}}33^{\text{s}}.241$ and $\delta(J2000)=-25^{\circ}17'18''.16$. Considering the small primary beam of $\sim 15''$ at 690 GHz and thus the increased need for accurate pointing, regular pointing offset updates (i.e., every ~ 3 h) were conducted on either 3C454.3 or 3C111 (using interferometry) or Jupiter (using single-dish measurements) throughout the night at 345 GHz. All spectral windows covered 2GHz in bandwidth, and the lower sideband (LSB) of the lower frequency was tuned to the $^{12}\text{CO}(J=3-2)$ line so that the $\text{HCO}^+(J=4-3)$ line fell into the corresponding upper sideband (USB), situated 10 GHz above the LSB. The USB of the 690 GHz receivers were tuned to the $^{12}\text{CO}(J=6-5)$ line leaving the corresponding LSB for continuum measurements. The weather was excellent with a 225 GHz atmospheric opacity of $\sim 0.05-0.1$ throughout the track. This corresponds to single sideband (SSB) system temperatures of $T_{\text{sys}}(\text{SSB})=5000-10000$ K at 690 GHz and $T_{\text{sys}}(\text{SSB})=400-800$ K at 345 GHz. We used the nearby ($\sim 20^\circ$ from NGC 253) planet Uranus as bandpass, gain and absolute flux calibrator. The calibration on Uranus was performed using a disk model to compensate for the fact that it was slightly resolved. The quality of the gain calibration was verified against a nearby quasar (J2348-

⁶ Further analysis of the $\text{HCO}^+(J=4-3)$ data may be presented separately, while this paper is concerned only with the ^{12}CO transitions

1631) which was observed with the same cycle times as Uranus. It appears to be of symmetric Gaussian shape at both frequencies but slightly shifted ($\sim +0.8''$) in Declination from its phase center at 690 GHz while being centered correctly at 345 GHz after applying the gain calibration. The spatial shift at 690 GHz indicates a problem with the phase transfer at 690 GHz, probably due to uncertainties in the measured baseline and/or larger distance of NGC 253 to the phase calibrator; the baseline error is around 0.3λ at 690 GHz. We hence consider this effect as a systematic instrumental and calibrational artifact and correct the data for this $\sim 0.8''$ shift. A similar positional shift was found for the 690 GHz SMA observations of Arp 220 that was also attributed to baseline errors by Matsushita et al. (2009). The accuracy of the flux calibration is estimated to be within 30% at 690 GHz and $\sim 20\%$ at 345 GHz.

Angular resolutions of $4''.2 \times 2''.1$ at position angle $\text{PA}=162^\circ$ are obtained at 690 GHz and of $5''.8 \times 4''.2$ at $\text{PA}=173^\circ$ at 345 GHz. We reach an rms noise level of $1\sigma=100$ mJy beam $^{-1}$ channel $^{-1}$ at 345 GHz and of $1\sigma=7$ Jy beam $^{-1}$ channel $^{-1}$ at 691 GHz per individual mosaic field and for a spectral resolution of 12 km s $^{-1}$. Note that we used a Nyquist sampling to place the mosaic fields based on the 690 GHz field of view so that in the combined mosaic maps at 690 GHz the noise distribution is not homogeneous and will increase toward the edges and be a factor of $\sqrt{2}$ smaller in the overlap regions; the mosaic fields at 345 GHz will, however, overlap by a much larger fraction so that the noise distribution is much more homogeneous there. The latter fact has been taken into account in our estimate of the 1σ levels for each figure (see their captions). A log of the observations is given in Table 1.

We subtracted the strong continuum emission found in NGC253, averaged over all line-free channels in each sideband, from the original data cubes to generate pure line emission data.

2.2. Previous SMA observations of $^{12}\text{CO}(J=3-2)$ and $^{12}\text{CO}(J=2-1)$

In order to enable a direct comparison between the $^{12}\text{CO}(J=6-5)$ emission and the lower-J CO emission and reduce systematic biases such as resolution effects due to different synthesized beams and uv-coverages, we merged our $^{12}\text{CO}(J=3-2)$ data with the high spectral resolution data at 345 GHz presented by Sakamoto et al. (2011). In the merged $^{12}\text{CO}(J=3-2)$ data set we then reach an rms noise level of $1\sigma=80$ mJy beam $^{-1}$ channel $^{-1}$ per mosaic field or ~ 60 mJy beam $^{-1}$ channel $^{-1}$ in the center of the mosaic for a spectral resolution of 12 km s $^{-1}$. We also included the $^{12}\text{CO}(J=2-1)$ data by Sakamoto et al. (2011) and Sakamoto et al. (2006) which is already a combination of low and high spatial resolution observations; the rms is found to be 25 mJy beam $^{-1}$ channel $^{-1}$ (using only a single field) at a spectral resolution of 12 km s $^{-1}$. In order to match the resolution of $^{12}\text{CO}(J=3-2)$ and $^{12}\text{CO}(J=2-1)$ to that of $^{12}\text{CO}(J=6-5)$, we used a uv-taper, obtaining an angular resolution of $4''.2 \times 2''.1$. We did not find significant differences with this method compared to matching⁷ the uv-coverages of the $^{12}\text{CO}(J=3-2)$ and $^{12}\text{CO}(J=2-1)$ data to that of $^{12}\text{CO}(J=6-5)$. In or-

⁷ i.e., restricting the uv-coverages to the overlapping regions

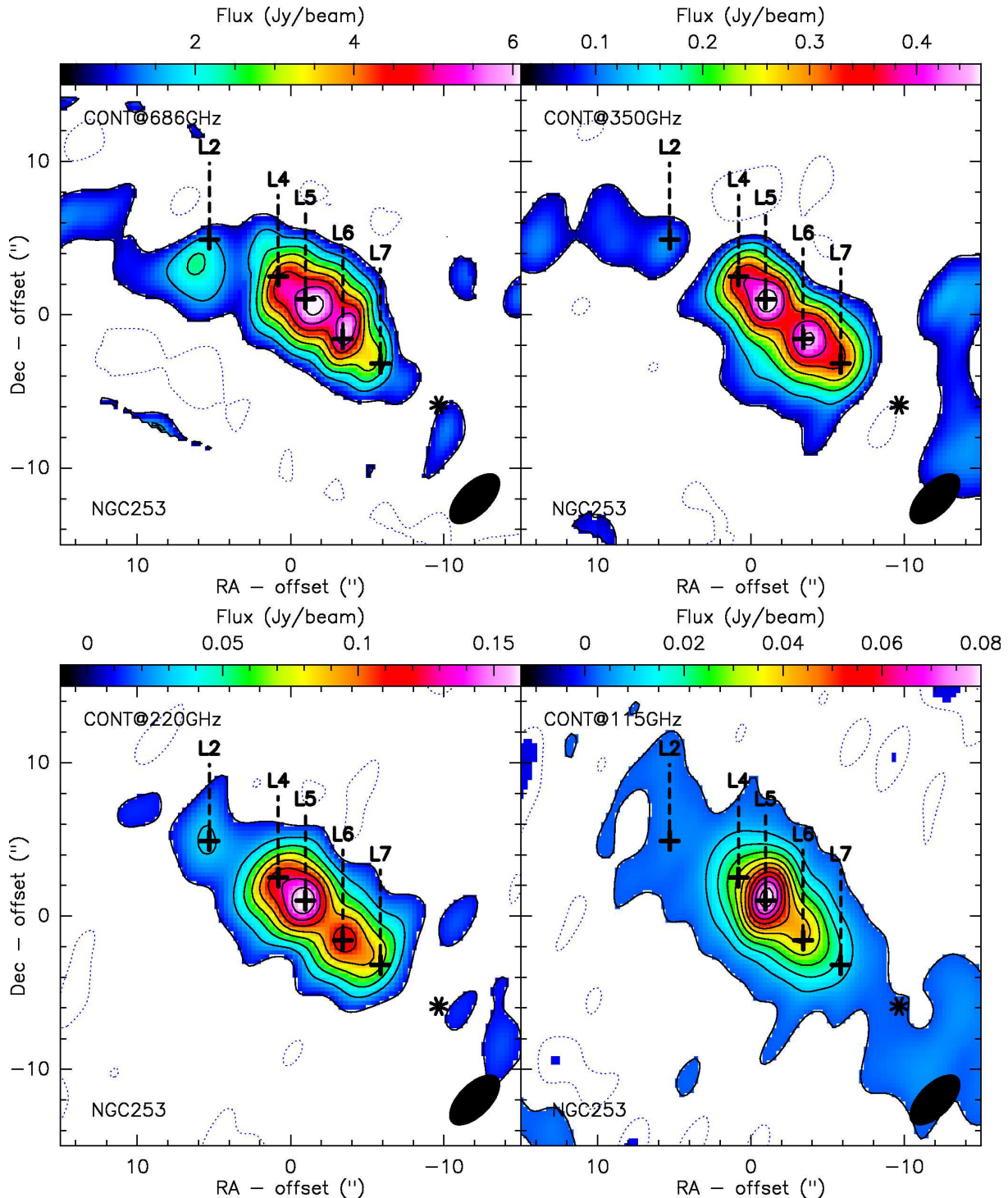


FIG. 1.— Continuum emission at 686 GHz (panel 1, *upper left*), 350 GHz (panel 2, *upper right*), 220 GHz (panel 3, *lower left*) and 115 GHz (panel 4, *lower right*), all at a spatial resolution of $\sim 4.2'' \times 2.1''$. The contours of the 686 GHz continuum emission start at -2σ , $2\sigma=0.76 \text{ Jy beam}^{-1}$ in steps of 2σ , those of the 350 GHz continuum emission start at -5σ , $10\sigma=0.064 \text{ Jy beam}^{-1}$ and go then in steps of 10σ , those of the 220 GHz continuum emission start at -3σ , $5\sigma=0.01 \text{ Jy beam}^{-1}$ and go in steps of 10σ , and those of the 115 GHz continuum emission start at -10σ , $10 \sigma=1.5 \text{ mJy beam}^{-1}$ and go in steps of 50σ . The black crosses indicated in each panel mark the positions of the respective line emission peaks defined in Fig. 4 matching those of the continuum peaks shown here and being in good agreement with the 1.3 mm continuum emission peaks from Sakamoto et al. (2011). The black star marks the position of the western superbubble/shell from Sakamoto et al. (2006). Note, that the eastern superbubble/shell lies outside the maps and is not shown here since no continuum emission is detected around it. The $(0'', 0'')$ offset is relative to the following absolute position: $\alpha(J2000)=00^{\text{h}}47^{\text{m}}33^{\text{s}}.241$ and $\delta(J2000)=-25^{\circ}17'18''.16$.

der to preserve the data in its entirety, we hence chose the first method.

2.3. ALMA observations of $^{12}\text{CO}(J=1-0)$

ALMA cycle 0 observations are available for the $^{12}\text{CO}(J=1-0)$ line from the ALMA science archive, that were done in the compact configuration with up to 19 antennas (project id: 2011.0.00172.S; see also Bolatto et al.

TABLE 3
PEAK FLUXES FOR THE INDIVIDUAL CONTINUUM PEAKS

ID	686 GHz ^a (mJy b ⁻¹)	350 GHz ^a (mJy b ⁻¹)	220 GHz ^a (mJy b ⁻¹)	115 GHz ^a (mJy b ⁻¹)
L2	1700±400	114±6	33±2	3±0.15
L4	4000±400	326±6	115±2	28±0.15
L5	5800±400	474±6	166±2	81±0.15
L6	5900±400	456±6	121±2	40±0.15
L7	2900±400	330±6	076±2	14±0.15

^a Errors are based on noise levels; b=beam (with a synthesized matched beam of $4''2\times2''1$ for all frequencies).

(2013)). The $^{12}\text{CO}(J=1-0)$ line was tuned to the USB within a 2 GHz large spectral window using a spectral resolution of 488 kHz ($\simeq 1.3 \text{ km s}^{-1}$). Uranus was used as absolute flux calibrator, J2333-237 as a band-pass calibrator and J0137-245 as phase and amplitude calibrator. Using the strong continuum emission, self-calibration was applied to the phases to improve the image quality of the continuum and line maps. Given the excellent uv-coverage, we used a slight uv-taper to smooth the initial spatial resolution to the angular resolution of our $^{12}\text{CO}(J=6-5)$ observations. Data reduction was done using CASA but further image processing was done in GILDAS. As with the other datasets, the continuum was derived from the line free channels and then subsequently subtracted from the channels containing both line and continuum emission.

2.4. Effects of Spatial Filtering

In order to assess the lack of short spacings and hence missing flux, we have compared our observations with existing single dish observations. Bayet et al. (2004) have observed the $^{12}\text{CO}(J=6-5)$ emission in NGC 253 using the Caltech Submillimeter Observatory (CSO). In the central $10.5''$, they obtain an integrated intensity of $1394\pm 279 \text{ K km s}^{-1}$, which corresponds to $\sim(55000\pm 11000) \text{ Jy km s}^{-1}$ assuming a conversion factor of $S/T_{\text{mb}}=39 \text{ Jy/K}$. The SMA observations yield an integrated line intensity of $\sim 45000 \text{ Jy km s}^{-1}$ in the central $10.5''$, a bit less than that from the single-dish observations but still within the large uncertainties ($\sim 20\text{-}30\%$) in both measurements. For the $^{12}\text{CO}(J=3-2)$ line emission, we find integrated line intensities of $\sim 45000 \text{ Jy km s}^{-1}$ in the central $\sim 20''$ very similar to those obtained from the single-dish measurements in the same area discussed in Bayet et al. (2004). Hence, the SMA observations did not resolve out significant emission from the $^{12}\text{CO}(J=3-2)$ and $^{12}\text{CO}(J=6-5)$ lines (at least within the central $\sim 10\text{-}20''$)⁸.

The $^{12}\text{CO}(J=1-0)$ was observed by Houghton et al. (1997) using the SEST telescope. They derive an integrated intensity of 377 K km s^{-1} in the central $\sim 30''$ of NGC 253. Using a conversion factor of $S/T_{\text{mb}}=19 \text{ Jy/K}$, this translates into $7100 \text{ Jy km s}^{-1}$. We find $\sim 7000 \text{ Jy km s}^{-1}$ in the central $\sim 30''$ as well, indicating that no flux has been resolved out with ALMA, at least in the center of NGC 253.

3. RESULTS & DISCUSSION

⁸ Note that no single-dish observations exist to cover the entire area of the 5-point mosaic observations conducted for this paper. The estimates of resolution effects are hence only for the central disk not covering the two outer shells

3.1. Continuum Emission

In our new SMA observations, continuum emission has been detected at 345 GHz (LSB), 355 GHz (USB), 681 GHz (LSB) and 691 GHz (USB) and is consistent between the two sidebands accounting for the frequency difference of 10 GHz between the sidebands. The upper left panel of Fig. 1 shows the sideband-averaged continuum emission at 686 GHz, the upper right panel shows 350 GHz (merged with the data from Sakamoto et al. (2011)), the lower left panel that of 220 GHz and the lower right panel that of 115 GHz. As mentioned before, all four continuum images were made with the same angular resolution. The distribution of the continuum emission is fairly similar amongst the four frequencies. The 686 GHz emission shows the same peaks as previously identified by Sakamoto et al. (2011) at higher angular resolution, marked with black crosses in Fig. 1. We labelled them L2 to L7 in this paper to facilitate a comparison to the line emission as the continuum peaks agree well in position with the corresponding line peaks (see definitions in Fig. 4). L5 and L6 appear to be slightly closer together at 686 GHz than at the lower frequencies and L2 is somewhat offset in Declination, i.e., $\sim 2''$ (\simeq half the synthesized beam), at 686 GHz than at the lower frequencies. This discrepancy is larger than the uncertainties in the absolute and relative positions of the peaks and might suggest a region of warmer dust close to L2. Indeed, Bradford et al. (2003) identified an overabundance of $^{12}\text{CO}(J=7-6)$ in the same region as well. The brightnesses of the different peaks, and their respective ratios to each other are very similar along the five continuum peaks, with L5 being the strongest, followed by L6, L4, L7 and L2.

Table 2 lists the total continuum fluxes for all four frequencies and Table 3 the individual fluxes per beam for each continuum peak. Assuming no significant resolution effects, the different fluxes indicate a total spectral index of +3 (for $S_\nu \propto \nu^\alpha$), see also Fig. 2. This is consistent with the spectral index found between the 1.3 mm and 0.87 mm continuum emission by Sakamoto et al. (2011) and between the 2.6 mm and 1.3 mm continuum by Sakamoto et al. (2006). This strongly indicates that the emission at >115 GHz is largely dominated by thermal dust emission. Our new 690 GHz data, along with the ALMA 115 GHz data, now reveal differences in continuum intensity ratios among the continuum peaks (see Fig. 2 and Fig. 3); Fig. 2 shows the spectral emissivity index maps between the different frequencies and Fig. 3 plots the continuum SED for each of the continuum peaks normalized to the peak flux at 220 GHz for each component. While it is true that along L4-L7 the ratios do not change too much, yielding still an index around 3, at least for the higher frequencies, it increases to $\sim 4\text{-}5$ at L2 (see Fig. 2). This appears to be consistent with the overabundance of $^{12}\text{CO}(J=7-6)$ found by Bradford et al. (2003) suggesting a warmer dust component in this region. The latter would add to a higher flux of the 690 GHz continuum emission assuming a two temperature phase of the dust here. Also, we see a slight drop of the spectral index with respect to the 2.6 mm continuum which most likely indicates the increasing role of non-thermal synchrotron and thermal free-free continuum emission towards longer wavelengths (see Fig. 3); Heesen et al.

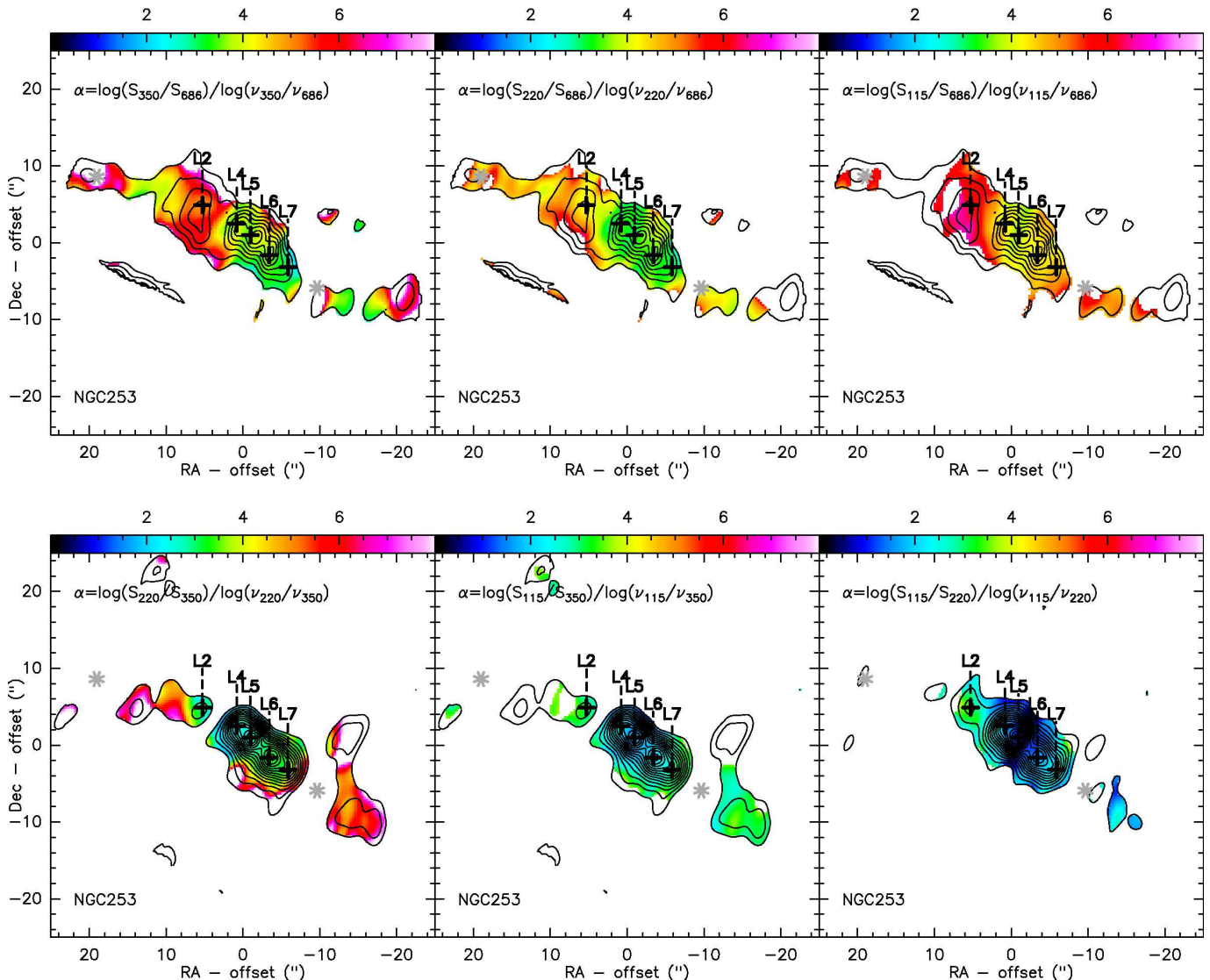


FIG. 2.— Spectral emissivity indices (labelled α in the images) derived from the continuum emission at 686 GHz, 350 GHz, 220 GHz and 115 GHz. The contours are the same as in Fig. 1 and are from the continuum emission at the frequency in the denominator, respectively. The grey stars and black crosses are the same as in Fig. 1.

(2011) and Ulvestad & Antonucci (1997) find a probably equal contribution between non-thermal synchrotron radio emission presumably from supernova remnants and thermal free-free radio emission from HII regions, i.e., star formation. Heesen et al. (2011) derive a spectral index of ~ -0.5 for the radio continuum emission at cm wavelengths in the center which steepens to -2 toward the outer parts and filaments. Judging from Figure 9 in Heesen et al. (2011), L5 and L6 show a spectral index of around -0.5 , while L2, L4 and L7 increase to around -1 , explaining the differences in the deviations of the 115 GHz continuum from the thermal (sub)mm (modified black body) slope for the different components. Depending on the component and assumed spectral index, the synchrotron/free-free emission contributes between 15% and 80% to the 115 GHz continuum emission, with L2 having the least (15%) and L5 and L7 ($\sim 80\%$) having the most contribution from these radio (cm/mm) processes to their 2.6 mm continuum emission. However, if the synchrotron/free-free spectral indices are somewhat flatter or steeper, the fraction of this emission to the total continuum emission will change accord-

ingly (being higher or lower, respectively). Given that generally (but not exclusively) the radio spectra of non-thermal synchrotron continuum emission is steeper (i.e., $\alpha \simeq -0.5$ to -1) than that of the thermal free-free continuum emission, it might be likely that the continuum emission at 2.6 mm has a larger contribution of thermal free-free emission (see also Peel et al. 2011). However, this might change from clump to clump within the disk and we have no actual way to distinguish between non-thermal synchrotron and thermal free-free emission from our continuum observations other than the spectral radio index (which might be misleading). Therefore, we will not further stress a differentiation between the two processes.

3.1.1. Temperature, opacity and mass of the dust

While fitting a simple power law to the (sub-)millimeter dust emission is a reasonable first-order approach, we can actually do better and determine the temperature, opacity and dust mass from our observations, using standard equations (for a comparison on similar observations and sources see also the recent work on

TABLE 4
MOLECULAR CLOUD COMPLEXES IN ALL OBSERVED ^{12}CO TRANSITIONS.

ID (1)	Bluest Gaussian Line				Central Gaussian Line				Reddest Gaussian Line				$\sum_{i=1}^3 (I_{i,\nu}^{\text{peak}})$ (14)
	$S_{1,\nu}^{\text{peak}}$ (2)	$I_{1,\nu}^{\text{peak}}$ (3)	v_0 (4)	Δv (5)	$S_{2,\nu}^{\text{peak}}$ (6)	$I_{2,\nu}^{\text{peak}}$ (7)	v_0 (8)	Δv (9)	$S_{3,\nu}^{\text{peak}}$ (10)	$I_{3,\nu}^{\text{peak}}$ (11)	v_0 (12)	Δv (13)	
$^{12}\text{CO}(J=6-5)$													
L0	—	—	—	—	<5.0	<426	-97	80	12.3± 2.8	1699± 406	-26	130	1699± 406
L1	—	—	—	—	6.1± 2.3	846± 324	-102	130	26.6± 2.6	2860± 398	-40	101	3706± 513
L2	<5.00	<346	-152	65	35.2± 1.8	3937± 424	-64	105	15.7± 1.9	1402± 240	38	84	5339± 487
L3	<5.00	<378	-129	71	27.5± 2.7	4218± 511	-50	144	5.0± 2.6	663± 350	32	124	4881± 619
L4	<5.00	<266	-110	50	32.0± 2.5	4767± 509	-52	140	22.9± 2.4	2684± 376	40	110	7451± 633
L5	<5.00	<266	-120	50	15.8± 2.6	1377± 283	-81	82	41.7± 1.7	5327± 496	22	120	6704± 571
L6	<5.00	<160	-91	30	48.2± 2.4	4618± 564	6	90	14.6± 2.7	1165± 264	95	75	5783± 623
L7	—	—	—	—	25.6± 2.2	2450± 342	12	90	<5.0	<426	112	80	2450± 342
L8	<5.00	<378	-26	71	5.4± 2.0	420± 166	50	73	<5.0	<415	126	78	420± 166
$^{12}\text{CO}(J=3-2)$													
L0	—	—	—	—	2.9± 0.2	249± 37	-97	80	3.0± 0.2	408± 40	-26	130	657± 54
L1	—	—	—	—	1.5± 0.2	207± 39	-102	130	15.4± 0.3	1654± 167	-40	101	1861± 171
L2	2.45± 0.2	169± 31	-152	65	13.9± 0.2	1559± 150	-64	105	7.1± 0.2	635± 78	38	84	2363± 172
L3	1.96± 0.4	148± 34	-129	71	11.8± 0.3	1811± 135	-50	144	2.9± 0.3	386± 51	32	124	2345± 148
L4	3.81± 0.4	203± 47	-110	50	13.0± 0.3	1938± 145	-52	140	4.5± 0.3	525± 59	40	110	2666± 163
L5	1.45± 0.4	77± 25	-120	50	9.3± 0.3	815± 103	-81	82	16.4± 0.2	2092± 176	22	120	2984± 205
L6	2.44± 0.6	78± 32	-91	30	21.3± 0.3	2042± 229	6	90	8.9± 0.4	714± 100	95	75	2834± 252
L7	—	—	—	—	16.5± 0.2	1583± 177	12	90	5.4± 0.2	457± 59	112	80	2040± 187
L8	1.50± 0.2	113± 20	-26	71	8.7± 0.2	678± 94	50	73	2.7± 0.2	222± 31	126	78	1013± 101
$^{12}\text{CO}(J=2-1)$													
L0	—	—	—	—	4.2± 0.1	360± 46	-97	80	2.1± 0.1	291± 24	-26	130	651± 52
L1	—	—	—	—	2.8± 0.1	383± 34	-102	130	12.6± 0.1	1357± 135	-40	101	1740± 139
L2	4.08± 0.1	282± 44	-152	65	12.2± 0.1	1362± 130	-64	105	5.6± 0.1	496± 60	38	84	2140± 150
L3	4.10± 0.2	310± 46	-129	71	8.3± 0.2	1279± 92	-50	144	3.6± 0.2	479± 44	32	124	2068± 112
L4	4.27± 0.2	227± 47	-110	50	9.1± 0.2	1353± 99	-52	140	6.2± 0.2	725± 68	40	110	2305± 129
L5	3.85± 0.2	205± 43	-120	50	5.2± 0.2	454± 58	-81	82	13.2± 0.1	1688± 142	22	120	2347± 159
L6	1.19± 0.1	38± 13	-91	30	17.7± 0.1	1696± 189	6	90	6.9± 0.1	550± 74	95	75	2284± 203
L7	—	—	—	—	14.2± 0.2	1360± 152	12	90	4.0± 0.2	344± 45	112	80	1704± 159
L8	1.25± 0.1	95± 15	-26	71	9.3± 0.1	720± 99	50	73	2.6± 0.1	219± 29	126	78	1034± 104
$^{12}\text{CO}(J=1-0)$													
L0	--	--	--	--	0.30±0.01	25± 3	-97	80	0.03±0.01	5± 2	-26	130	30± 4
L1	--	--	--	--	0.16±0.02	22± 3	-102	130	1.84±0.02	197± 20	-40	101	219± 20
L2	0.34±0.04	23± 4	-152	65	1.66±0.03	185± 18	-64	105	0.44±0.03	40± 6	38	84	248± 19
L3	0.42±0.04	32± 5	-129	71	1.11±0.03	171± 13	-50	144	0.17±0.03	22± 4	32	124	225± 14
L4	0.63±0.06	34± 8	-110	50	1.45±0.04	216± 17	-52	140	0.58±0.04	68± 8	40	110	318± 20
L5	0.43±0.05	23± 5	-120	50	0.77±0.04	67± 9	-81	82	1.67±0.03	213± 18	22	120	303± 21
L6	0.06±0.04	2± 1	-91	30	2.57±0.04	246± 28	6	90	0.95±0.04	76± 11	95	75	322± 30
L7	--	--	--	--	1.96±0.03	188± 21	12	90	0.51±0.03	43± 6	112	80	231± 22
L8	0.08±0.01	6± 1	-26	71	1.20±0.01	93± 13	50	73	0.31±0.01	26± 4	126	78	125± 14

(1) Names of $^{12}\text{CO}(J=6-5)$ line emission peaks as given in this paper (starting with an L). Corresponding $^{12}\text{CO}(J=3-2)$ and $^{12}\text{CO}(J=2-1)$ names from Sakamoto et al. (2011): L0=SB2; L2≈Sa1; L4≈Sa2; L5≈Sa3; L6≈Sa4; L7≈Sa5; L8=SB1. The absolute positions of each of these line peaks are (for $\alpha=00^{\text{h}}47^{\text{m}}$, $\delta=-25^{\circ}17'$): L0=34.56s,09.2"; L1=34.07s,12.0"; L2=33.69s,14.2"; L3=33.54s,14.5"; L4=33.31s,15.8"; L5=33.15s,17.5"; L6=32.97s,19.4"; L7=32.80s,21.7"; L8=32.53s,24.0".

(2,3,6,7,10,11) Peak flux densities S_{ν} (in Jy beam^{-1}) and spectrally integrated intensities $I_{i,\nu}$ ($=\int (S_{i,\nu}^{\text{int}} dv)$) in ($\text{Jy beam}^{-1} \text{ km s}^{-1}$) derived at the peak emission for each fitted Gaussian line.

(4,8,12) Zero velocity is with respect to the redshifted frequency of the observed CO line transition. The central velocities of each Gaussian line component have been first derived by fitting the $^{12}\text{CO}(J=2-1)$ and $^{12}\text{CO}(J=3-2)$ lines. The so found values have been averaged and subsequently fixed for each fit. We assume a 5-10 km s^{-1} error on the central velocities. The unit is km s^{-1} .

(5,9,13) Full width at half maximum (FWHM) of each line. Identical to the velocity centre, the FWHM have been first derived by fitting the $^{12}\text{CO}(J=2-1)$ and $^{12}\text{CO}(J=3-2)$ lines, taking the mean of both and subsequently fixing it in the fits for all line transition. We assume an error on the FWHM of 5-10 km s^{-1} . The unit is in km s^{-1} .

690 GHz ALMA data for Arp220 by Wilson et al. 2014; Scoville et al. 2015). By using flux ratios, we can eliminate some assumptions such as on the dust emissivity, in particular to derive the dust opacities and dust temperatures (but see also further below for the dust mass for which this approach does not work). This gives the following equation (see also Wilson et al. 2014):

$$\frac{S_{\nu_1}}{S_{\nu_2}} = \left(\frac{\nu_1}{\nu_2}\right)^3 \left(\frac{e^{h\nu_2/kT_d} - 1}{e^{h\nu_1/kT_d} - 1}\right) \left(\frac{1 - e^{-\tau_1}}{1 - e^{-\tau_2}}\right) \quad (1)$$

Using the flux densities of the emission at 220 GHz⁹, 350 GHz and 686 GHz, this allows us to derive the opacities and dust temperatures in the different peaks, as shown in Fig.3 along with the χ^2 -fits. We assumed a spectral index of the dust emissivity¹⁰ of 1.8 (see Wilson et al. 2014, and references therein) and varied the

⁹ Contributions from the free-free/synchrotron emission can be neglected here as they are less than 5% being hence smaller than the uncertainties and leaving unchanged the final best fit solutions.

¹⁰ We fitted equally for a spectral index of 1.5 and 2.1 as used in previous publications for NGC 253 (e.g., Peel et al. 2011), but the best fit solutions were found for a value of 1.8

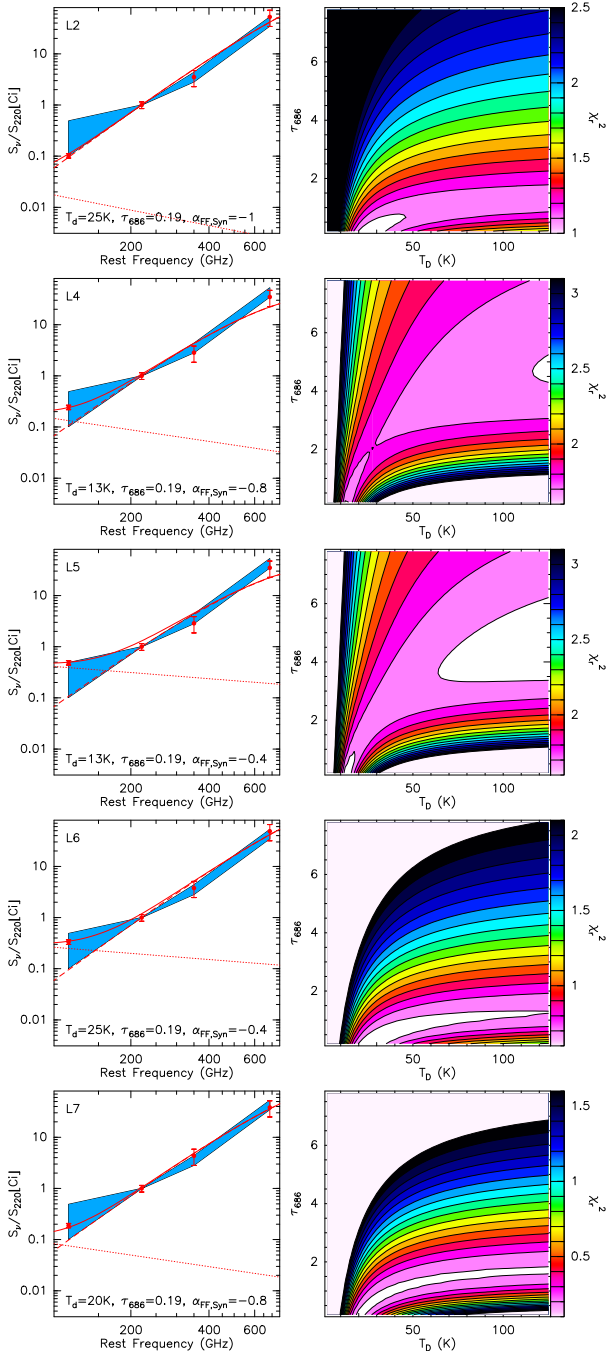


FIG. 3.— Continuum SED for the different continuum peaks (only peak fluxes taken for each frequency; *left panel*), normalised to the respective continuum fluxes at 230 GHz for each component (note the logarithmic scale of the flux ratio) and the corresponding best fit solution (i.e., lowest reduced χ_r^2 ; *right panel*) for each continuum peak assuming a dust emissivity of $\beta = 1.8$ (see text for more details). The dashed and dotted lines represent the thermal (from a modified black body) and non-thermal synchrotron plus thermal free-free contribution to the emission, while the solid line is the composite of both. The dashed line has been fitted to the data, while the dotted line was made using a fixed beta of 1.8 from Heesen et al. (2011) (there are not enough observational data to conduct a thorough fit for beta as well). The error bars correspond to $\pm 1\sigma$. The blue shaded areas plotted in each panel on the left indicate the range of continuum fluxes found at the positions of L2-L7, i.e., correspond to $\min(\text{flux}@(\text{L2-L7}))$ to $\max(\text{flux}@(\text{L2-L7}))$ at each wavelength. T_d is the dust temperature, τ_{686} is the opacity at 686 GHz and $\alpha_{\text{FF,Syn}}$ is the spectral index coming from the free-free/synchrotron emission.

dust temperatures in the range of 2.5 K up to 150 K and opacities at 220 GHz between 0.02 and 1 (corresponding to opacities at 686 GHz of $\tau_{686} = (\nu_{686}/\nu_{220})^{1.8} \cdot \tau_{220}$, i.e., ~ 0.15 to 8). The best-fit solutions suggest dust temperatures of ~ 10 -30 K at low opacities of $\tau_{686} = 0.19$ for all five peaks, with L2 having the highest T_d of 25 K. However, L4 and L5 have almost equally low- χ^2 solutions at higher $T_d > 60$ K and much higher opacities of $\tau_{686} = 4$ while the opacities of L2 stay consistently below 1. The two-temperature best-fit ranges are in good agreement with what is found for the molecular gas that can only be well fit with a two-phase temperature gas model (see next Sections). As dust and molecular gas are intimately bound, one would expect a two-temperature phase as well in the dust. The higher T_d of the inner disk are similar to the values found for the eastern nucleus in Arp 220 which was fitted to ~ 80 K but at higher opacities that are closer to the values found in the western nucleus of Arp 220 (Wilson et al. 2014).

To calculate the dust mass M_{dust} at a given frequency for each peak, we use the following standard equation:

$$M_{\text{dust}} = \frac{S_\nu D^2}{\kappa_\nu B(\nu, T_d)} \quad (2)$$

with S_ν being the flux observed at frequency ν , D the distance ($= 3.5$ Mpc), κ_ν the mass absorption coefficient $\kappa_\nu = \kappa_0(\nu/\nu_0)^\beta$ with β being the spectral index of the dust emissivity, and $B(\nu, T_d)$ the Planck function. Assuming $\beta = 1.8$ and $\kappa_{158\mu\text{m}} \simeq 0.6$ -3 m^2/g at a frequency of $\nu_0 = 1.9$ THz ($\equiv 158\mu\text{m}$) depending on the dust properties (see Hirashita et al. 2014; Dayal et al. 2010; Zubko et al. 1996, 2004; Draine & Lee 1984), we estimate dust masses of $\sim 10^4$ - 10^5 - M_\odot per dust peak, i.e. with an uncertainty of a factor of 5-10. The biggest uncertainty comes from the range of κ_ν that depends on which type or combination of dust grains dominates (i.e., graphite, silicate, amorphous carbon, etc., see for a summary Hirashita et al. 2014). Comparing the dust masses to the molecular gas masses derived from optically thin molecular tracers (such as ^{13}CO) of a few $\sim 10^7$ M_\odot (see for instance Leroy et al. 2015), we derive a gas-to-dust mass ratio of $\gtrsim 100$ -1000 for the different peaks and the range in κ . Doing the same exercise on the global flux of the entire disk, we find a dust mass of about a few $10^6 M_\odot$ for a dust temperature of $T_d = 25$ K. The gas mass of the disk in NGC253 is about a few 10^8 - 10^9 M_\odot in the area of the detected continuum emission, resulting in a global gas-to-dust mass ratio of a few hundred. The gas-to-dust mass ratios are consistent with the values (~ 100 -1000) usually found in active galaxies with metallicities around solar (see for instance Remy-Ruyer et al. 2014).

The global (and individual) dust temperatures found here are in good agreement with previous works on NGC 253 (see for instance Peel et al. 2011). The global dust mass of NGC 253 is similar to that found in nearby active galaxies (see for instance Remy-Ruyer et al. 2014) but one to two orders of magnitude smaller than that found for nearby (ultra-)luminous-infrared galaxies (=U)LIRGs) such as Arp 220, NGC 6240 or NGC 1614 (see for instance Scoville et al. 2015; Xu et al. 2015). Arp 220 and NGC 6240 show dust masses around a few $10^9 M_\odot$ and NGC 1614 has a dust mass around 10^7 - $10^8 M_\odot$. This is not surprising as especially the nuclei

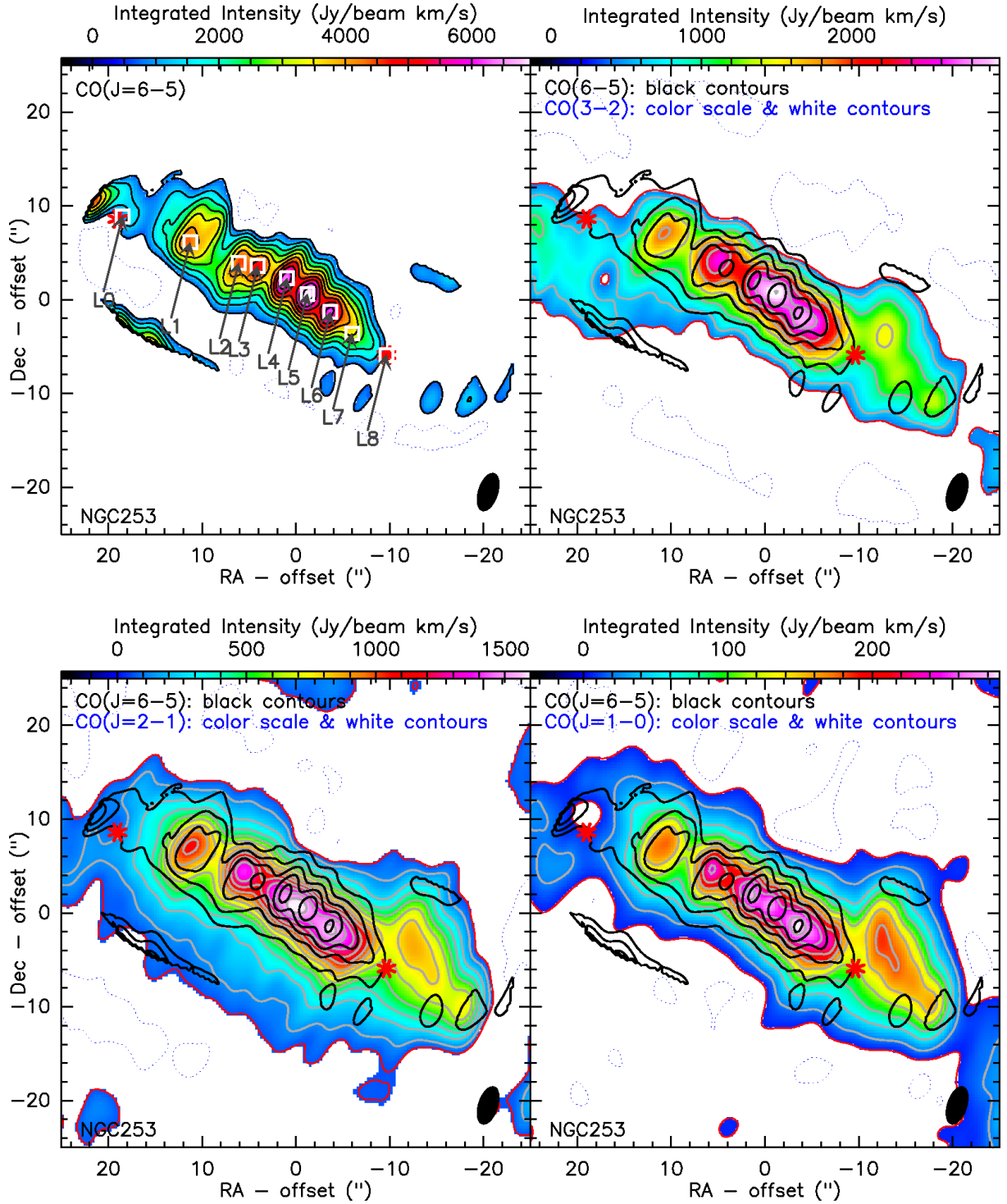


FIG. 4.— Panels comparing the flux distributions of the four ^{12}CO line transitions. Panel 1 (*upper left*) shows the $^{12}\text{CO}(J=6-5)$ emission in color scale and contours. Panel 2 (*upper right*) shows the $^{12}\text{CO}(J=3-2)$ emission (this paper and Sakamoto et al. (2011); in *color scale* and *red and grey contours*) overlaid with contours (in *black*) of the $^{12}\text{CO}(J=6-5)$ line emission. Panel 3 (*lower left*) shows the same but for the $^{12}\text{CO}(J=2-1)$ emission (taken from Sakamoto et al. 2011) overlaid with the contours of the $^{12}\text{CO}(J=6-5)$ emission. Panel 4 (*lower right*) shows the same but for the $^{12}\text{CO}(J=1-0)$ emission (taken from the ALMA science archive) overlaid with the contours of the $^{12}\text{CO}(J=6-5)$ emission. The red stars (inner and outer two white squares) mark the positions of the two shells (L0 and L8) from Sakamoto et al. (2006) and L1-L7 (*white squares*) with the corresponding arrows mark the line peaks of the $^{12}\text{CO}(J=6-5)$ emission in order to facilitate the discussion. The contours of the $^{12}\text{CO}(J=6-5)$ emission start at -3σ , $2\sigma=660 \text{ Jy km s}^{-1} \text{ beam}^{-1}$ in steps of 2σ (upper left panel, otherwise in steps of 4σ). The contours of the $^{12}\text{CO}(J=3-2)$ emission start at -20σ , $100\sigma=420 \text{ Jy km s}^{-1} \text{ beam}^{-1}$ in steps of 100σ . The contours of the $^{12}\text{CO}(J=2-1)$ emission start at -50σ , $50\sigma=64 \text{ Jy km s}^{-1} \text{ beam}^{-1}$ in steps of 100σ . The contours of the $^{12}\text{CO}(J=1-0)$ emission start at -25σ , $25\sigma=5 \text{ Jy km s}^{-1} \text{ beam}^{-1}$ in steps of 150σ .

in Arp 220 are known to be highly obscured exhibiting a starburst much stronger than that in the disk of NGC 253

while NGC 1614 is likely more comparable to NGC 253 than Arp 220.

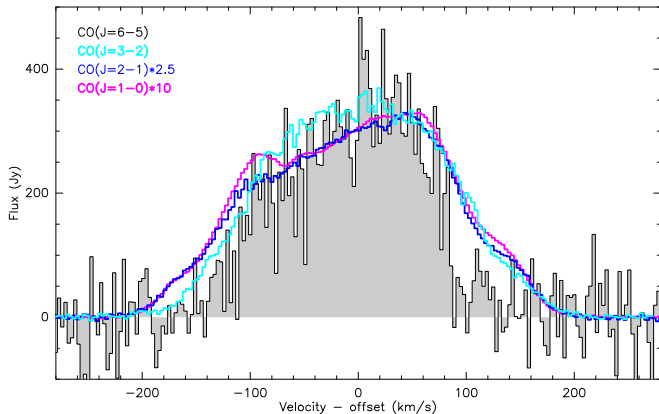


FIG. 5.— The flux of the four different line transitions integrated over the entire emission region, respectively. It is clear from the broad profile that several Gaussian components are present for each CO transition, indicating the presence of multiple molecular clouds or clumps at slightly different velocities. However the velocity range is similar for each line, indicating that the gas is co-spatial in the clumps.

3.2. Line Emission

3.2.1. General Properties

We clearly detect emission from $^{12}\text{CO}(J=6-5)$ (Fig. 4). The distribution of the spectrally integrated $^{12}\text{CO}(J=6-5)$ line emission closely follows that of $^{12}\text{CO}(J=3-2)$, $^{12}\text{CO}(J=2-1)$ and $^{12}\text{CO}(J=1-0)$ (see Fig. 4). We identify at least seven different peaks in the integrated $^{12}\text{CO}(J=6-5)$ emission, labeled L1 to L7 in Fig. 4, plus the location of the two shells labeled L0 (for SB2) and L8 (for SB1). L4 to L6 appear to be the most dominant ones in all four ^{12}CO transitions. L5 is spatially coincident with the dynamical center of NGC 253 (see Rosenberg et al. 2012; Müller-Sánchez et al. 2010). Most of these line peaks in the disk, with the exceptions of L1 and L3 which have no correspondence in the continuum emission, spatially coincide with the continuum peaks at 2.6 mm, 1.3 mm, 0.87 mm and 0.43 mm identified in Sakamoto et al. (2011) and this work (see also Section 3.1). Line peaks L4 and L5 appear merged for the $^{12}\text{CO}(J=3-2)$ and $^{12}\text{CO}(J=2-1)$ emission at the angular resolution used in this paper while they are clearly separated for the $^{12}\text{CO}(J=6-5)$ emission. However, at the higher angular resolution used in Sakamoto et al. (2011), the peak positions match well those seen for $^{12}\text{CO}(J=6-5)$, with the exception of L3, which does not have an obvious counterpart in the lower transitions. This merging of the peaks is probably due to extended emission in the lower ^{12}CO transitions as $^{12}\text{CO}(J=6-5)$ most likely traces denser (and/or hotter) gas. L5 appears to be the strongest peak for all lines except $^{12}\text{CO}(J=1-0)$, where L6 seems to dominate. Interestingly, L4 appears to be somewhat brighter in $^{12}\text{CO}(J=6-5)$, $^{12}\text{CO}(J=2-1)$ and $^{12}\text{CO}(J=1-0)$ than in $^{12}\text{CO}(J=3-2)$, an effect that is already seen for the $^{13}\text{CO}(J=2-1)$, $\text{C}^{18}\text{O}(J=2-1)$ and $\text{HCN}(J=4-3)$ emission by Sakamoto et al. (2011).

We only detect marginal $^{12}\text{CO}(J=6-5)$ emission around the western and eastern shells (SB1=L08 and SB2=L01) described in Sakamoto et al. (2006) and marked with stars and squares in Fig. 4. While the eastern shell is only partially covered with our five-point mosaic of the $^{12}\text{CO}(J=6-5)$ emission, the western shell is (almost) completely covered. However, the western

shell is already significantly weaker in the lower ^{12}CO transitions, so that we might still simply lack adequate sensitivity in our observations for a clear detection.

The line profiles of the $^{12}\text{CO}(J=6-5)$, $^{12}\text{CO}(J=3-2)$, $^{12}\text{CO}(J=2-1)$ and $^{12}\text{CO}(J=1-0)$ emission, shown in Fig. 5, were spatially integrated over the entire emission area for each transition respectively. Multiple-component (up to three) Gaussian fits were carried out on the line profiles and the results are given in Table 2. As can be seen, while overall the line profiles agree well with each other, part of the redshifted and blueshifted wing of the $^{12}\text{CO}(J=3-2)$, $^{12}\text{CO}(J=2-1)$ and $^{12}\text{CO}(J=1-0)$ line emission is apparently missing in the $^{12}\text{CO}(J=6-5)$ line emission. These “wing”-components are most likely associated with the western (redshifted velocities) and eastern (blueshifted velocities) shells (see Sakamoto et al. 2006). While the eastern part could easily still be hidden in the noise, one gets the impression that the redshifted $^{12}\text{CO}(J=6-5)$ emission is indeed not present and that this is more likely due to excitation effects than to insufficient sensitivity as also shown by the individual spectra at the peaks (see Fig. 7).

Looking at the velocity channel maps in Fig. 6, in which the $^{12}\text{CO}(J=6-5)$ emission is exemplary plotted in contours over the $^{12}\text{CO}(J=1-0)$ emission in color scale, we find again that all four transitions strongly resemble each other for most velocities; especially the three lowest transitions are almost indistinguishable from each other (see also Fig. 5 & 7). Although it is difficult to clearly identify the line peaks (Fig. 4) of the $^{12}\text{CO}(J=6-5)$ emission in the velocity resolved channels due to the lower signal-to-noise ratios and because each of these peaks represent an ensemble of giant molecular cloud complexes (GMCs), one can still see some trends. L6 clearly is the dominant and brightest peak for the $^{12}\text{CO}(J=3-2)$, $^{12}\text{CO}(J=2-1)$ and $^{12}\text{CO}(J=1-0)$ emission between velocities 24 km s^{-1} and 60 km s^{-1} with L4 and L5 being significantly weaker as opposed to the spectrally integrated maps in Fig. 4. At these velocities, both L5 and L6 appear almost equally bright in the $^{12}\text{CO}(J=6-5)$ emission. L3 and L4 also look equally strong in $^{12}\text{CO}(J=6-5)$ for velocities around -80 km s^{-1} and -48 km s^{-1} , while L3 seems to be brighter for the lower transitions. The lack of significant $^{12}\text{CO}(J=6-5)$ emission at the higher velocities ($\gtrsim 100 \text{ km s}^{-1}$ and $\lesssim -100 \text{ km s}^{-1}$) with respect to the lower three transitions is again striking.

Figure 7 shows the line spectra taken at the position of each line peak for the four different ^{12}CO transitions. Again, the similar shape of the profiles amongst all four transitions for each peak is striking. This is strong evidence that all four transitions trace the same molecular gas, i.e., the same molecular clumps along the disk of NGC 253. We fitted a multiple-component (up to three) Gaussian to all line profiles. The results of these fits are given in Table 4. To reduce the parameter space for the fit and to rest consistent between the fits for each transition, we fixed the line centers of the three different line components by choosing the best compromise for the line centers between the three lowest transition after an initial fit to them with the line center as free parameter. In Figure 7 it becomes clear why L6 appears stronger in the velocity channel maps compared to L5 in the spectrally integrated map: L5 is weaker but with a much broader line profile than L6. Judging also from these complex line

TABLE 5
 ^{12}CO BRIGHTNESS TEMPERATURE RATIOS FROM INDIVIDUAL GAUSSIAN COMPONENTS

Ratio (1)	L0 (2)	L1 (3)	L2 (4)	L3 (5)	L4 (6)	L5 (7)	L6 (8)	L7 (9)	L8 (10)
Bluest Gaussian Line									
R_{65}^{32}	–	–	>2.00	>1.60	>3.10	>1.20	>1.90	–	>1.20
R_{65}^{21}	–	–	>7.30	>7.40	>7.70	>6.90	>2.10	–	>2.30
R_{65}^{10}	–	–	>2.40	>3.00	>4.60	>3.10	>0.4	–	>0.60
R_{32}^{21}	–	–	3.80 ± 0.90	4.70 ± 1.30	2.50 ± 0.80	6.00 ± 2.30	1.10 ± 0.60	–	1.90 ± 0.40
R_{32}^{10}	–	–	1.20 ± 0.30	1.90 ± 0.50	1.50 ± 0.50	2.70 ± 1.10	0.20 ± 0.10	–	0.50 ± 0.10
R_{21}^{10}	–	–	0.33 ± 0.08	0.41 ± 0.09	0.60 ± 0.19	0.45 ± 0.14	0.21 ± 0.13	–	0.25 ± 0.06
R_{65}^{32}/R_{L4}	–	–	–	–	–	–	–	–	–
R_{65}^{21}/R_{L4}	–	–	–	–	–	–	–	–	–
R_{65}^{10}/R_{L4}	–	–	–	–	–	–	–	–	–
R_{32}^{21}/R_{L4}	–	–	1.5 ± 0.6	1.9 ± 0.8	1.0	2.4 ± 1.2	0.4 ± 0.2	–	0.8 ± 0.3
R_{32}^{10}/R_{L4}	–	–	0.8 ± 0.3	1.3 ± 0.6	1.0	1.8 ± 0.9	0.2 ± 0.1	–	0.3 ± 0.1
R_{21}^{10}/R_{L4}	–	–	0.5 ± 0.2	0.7 ± 0.3	1.0	0.7 ± 0.3	0.4 ± 0.3	–	0.4 ± 0.2
Central Gaussian Line									
R_{65}^{32}	>2.30	1.00 ± 0.40	1.60 ± 0.20	1.70 ± 0.20	1.60 ± 0.20	2.40 ± 0.60	1.80 ± 0.30	2.60 ± 0.50	6.50 ± 2.70
R_{65}^{21}	>7.60	4.10 ± 1.60	3.10 ± 0.40	2.70 ± 0.40	2.60 ± 0.30	3.00 ± 0.70	3.30 ± 0.50	5.00 ± 0.90	15.40 ± 6.50
R_{65}^{10}	>2.10	0.90 ± 0.40	1.70 ± 0.20	1.50 ± 0.20	1.60 ± 0.20	1.80 ± 0.40	1.90 ± 0.30	2.80 ± 0.50	8.00 ± 3.30
R_{32}^{21}	3.30 ± 0.60	4.20 ± 0.90	2.00 ± 0.30	1.60 ± 0.20	1.60 ± 0.20	1.30 ± 0.20	1.90 ± 0.30	1.90 ± 0.30	2.40 ± 0.50
R_{32}^{10}	0.70 ± 0.10	1.00 ± 0.20	1.10 ± 0.10	0.80 ± 0.10	1.00 ± 0.10	0.70 ± 0.10	1.10 ± 0.20	1.10 ± 0.20	1.20 ± 0.20
R_{21}^{10}	0.20 ± 0.04	0.23 ± 0.04	0.54 ± 0.07	0.53 ± 0.06	0.64 ± 0.07	0.59 ± 0.11	0.58 ± 0.09	0.55 ± 0.09	0.52 ± 0.10
R_{65}^{32}/R_{L4}	>1.4	0.6 ± 0.3	1.0 ± 0.2	1.1 ± 0.2	1.0	1.5 ± 0.4	1.1 ± 0.2	1.6 ± 0.4	4.0 ± 1.8
R_{65}^{21}/R_{L4}	>3.0	1.6 ± 0.7	1.2 ± 0.2	1.1 ± 0.2	1.0	1.2 ± 0.3	1.3 ± 0.3	2.0 ± 0.4	6.0 ± 2.6
R_{65}^{10}/R_{L4}	>1.3	–	1.0 ± 0.2	0.9 ± 0.2	1.0	1.1 ± 0.3	1.2 ± 0.3	1.7 ± 0.4	4.9 ± 2.2
R_{32}^{21}/R_{L4}	2.1 ± 0.5	2.7 ± 0.6	1.3 ± 0.2	1.0 ± 0.1	1.0	0.8 ± 0.2	1.2 ± 0.2	1.2 ± 0.2	1.5 ± 0.3
R_{32}^{10}/R_{L4}	0.6 ± 0.1	1.0 ± 0.3	1.1 ± 0.2	0.8 ± 0.1	1.0	0.7 ± 0.1	1.1 ± 0.2	1.1 ± 0.2	1.2 ± 0.3
R_{21}^{10}/R_{L4}	0.3 ± 0.1	0.4 ± 0.1	0.9 ± 0.2	0.8 ± 0.1	1.0	0.9 ± 0.2	0.9 ± 0.2	0.9 ± 0.2	0.8 ± 0.2
Reddest Gaussian Line									
R_{65}^{32}	1.00 ± 0.20	2.30 ± 0.40	1.80 ± 0.40	2.30 ± 1.30	0.80 ± 0.10	1.60 ± 0.20	2.50 ± 0.70	>4.30	>2.10
R_{65}^{21}	1.50 ± 0.40	4.30 ± 0.70	3.20 ± 0.70	6.50 ± 3.50	2.40 ± 0.40	2.90 ± 0.40	4.20 ± 1.10	>7.30	>4.70
R_{65}^{10}	0.11 ± 0.05	2.50 ± 0.40	1.00 ± 0.20	1.20 ± 0.70	0.90 ± 0.20	1.40 ± 0.20	2.30 ± 0.60	>3.60	>2.30
R_{32}^{21}	1.60 ± 0.20	1.80 ± 0.30	1.80 ± 0.30	2.80 ± 0.40	3.10 ± 0.50	1.80 ± 0.20	1.70 ± 0.30	1.70 ± 0.30	2.20 ± 0.40
R_{32}^{10}	0.11 ± 0.04	1.10 ± 0.20	0.60 ± 0.10	0.50 ± 0.10	1.20 ± 0.20	0.90 ± 0.10	1.00 ± 0.20	0.80 ± 0.20	1.10 ± 0.20
R_{21}^{10}	0.07 ± 0.03	0.58 ± 0.08	0.32 ± 0.06	0.18 ± 0.04	0.38 ± 0.06	0.50 ± 0.06	0.55 ± 0.11	0.50 ± 0.10	0.47 ± 0.10
R_{65}^{32}/R_{L4}	1.2 ± 0.40	3.0 ± 0.7	2.3 ± 0.6	3.0 ± 1.7	1.0	2.0 ± 0.4	3.1 ± 1.0	>5.5	>2.7
R_{65}^{21}/R_{L4}	0.6 ± 0.20	1.8 ± 0.4	1.3 ± 0.3	2.7 ± 1.5	1.0	1.2 ± 0.3	1.7 ± 0.5	>3.0	>2.0
R_{65}^{10}/R_{L4}	0.1 ± 0.05	2.7 ± 0.7	1.1 ± 0.3	1.3 ± 0.8	1.0	1.6 ± 0.4	2.6 ± 0.8	>4.0	>2.5
R_{32}^{21}/R_{L4}	0.5 ± 0.10	0.6 ± 0.1	0.6 ± 0.1	0.9 ± 0.2	1.0	0.6 ± 0.1	0.6 ± 0.1	0.5 ± 0.1	0.7 ± 0.2
R_{32}^{10}/R_{L4}	0.1 ± 0.04	0.9 ± 0.2	0.5 ± 0.1	0.4 ± 0.1	1.0	0.8 ± 0.2	0.8 ± 0.2	0.7 ± 0.2	0.9 ± 0.2
R_{21}^{10}/R_{L4}	0.2 ± 0.09	1.5 ± 0.3	0.9 ± 0.2	0.5 ± 0.1	1.0	1.3 ± 0.2	1.5 ± 0.4	1.3 ± 0.3	1.3 ± 0.3

(1-10) *First six rows:* Brightness temperature ratios between the different ^{12}CO transitions derived for each line peak (Table 2). We converted all ^{12}CO integrated peak intensities from Jansky to Kelvin. *Rows seven to twelve:* Brightness temperature ratios with respect to peak L4, respectively.

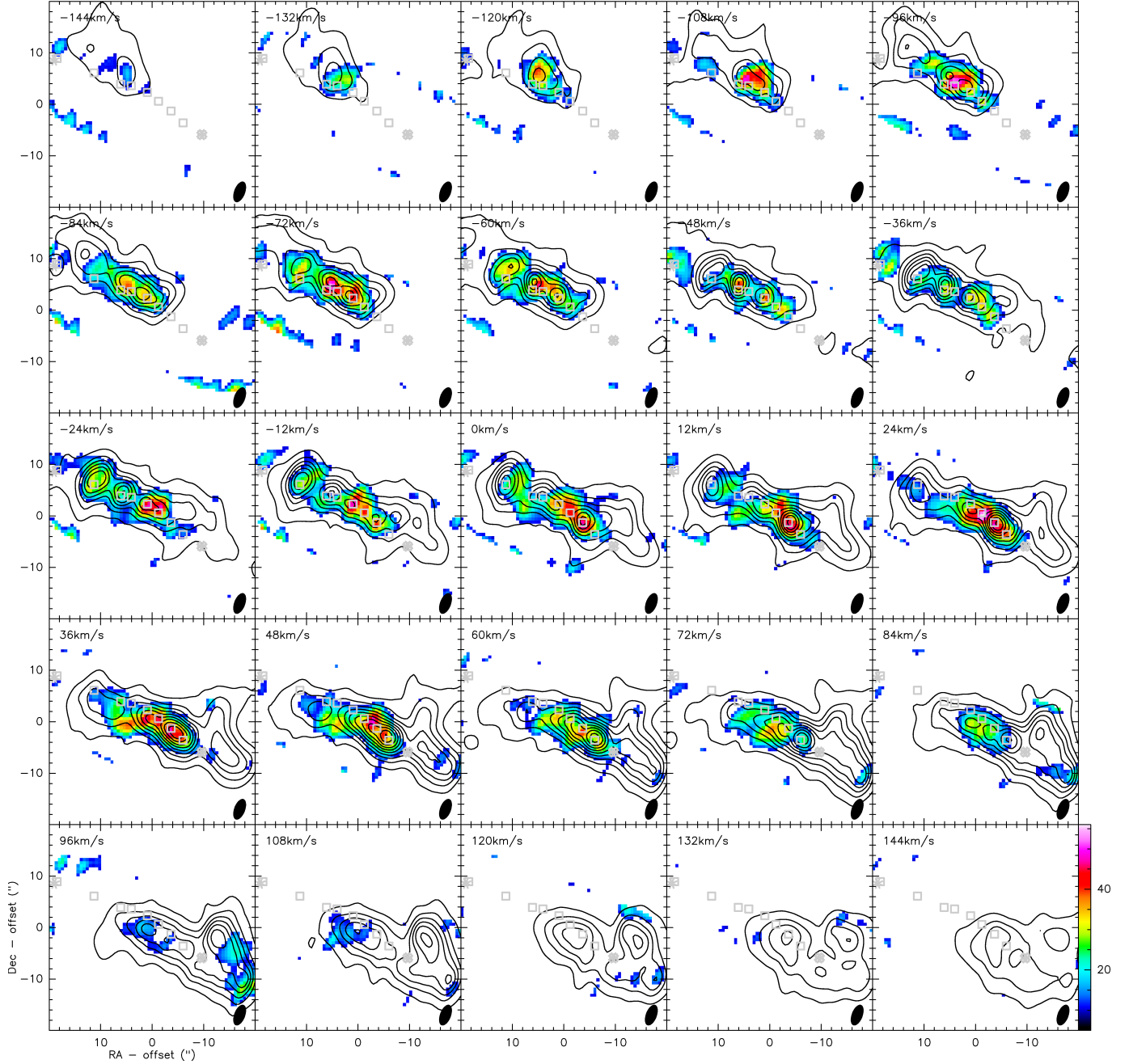


FIG. 6.— Channel maps of the $^{12}\text{CO}(J=1-0)$ (black contours) overlaid onto the $^{12}\text{CO}(J=6-5)$ emission (color scale). The spectral resolution is $\sim 12 \text{ km s}^{-1}$. The contours for the $^{12}\text{CO}(J=1-0)$ emission start at $100\sigma=0.1 \text{ Jy beam}^{-1} \text{ channel}^{-1}$ and go in steps of 300σ . The grey symbols represent the seven different line peaks in the disk and the stars the two shells as shown in Fig. 4 and specified in Table 4.

TABLE 6
 ^{12}CO BRIGHTNESS TEMPERATURE RATIOS DERIVED FROM THE SUM OF INDIVIDUAL GAUSSIAN COMPONENTS.

Ratio (1)	L0 (2)	L1 (3)	L2 (4)	L3 (5)	L4 (6)	L5 (7)	L6 (8)	L7 (9)	L8 (10)
R_{65}^{32}	1.50±0.40	2.00±0.30	1.80±0.20	1.90±0.30	1.40±0.10	1.80±0.20	2.00±0.30	3.30±0.60	9.60±3.90
R_{65}^{21}	3.40±0.90	4.20±0.70	3.60±0.40	3.80±0.50	2.80±0.30	3.10±0.30	3.60±0.50	6.30±1.10	22.10±9.00
R_{65}^{10}	0.60±0.20	2.10±0.40	1.70±0.20	1.70±0.20	1.50±0.20	1.60±0.20	2.20±0.30	3.40±0.60	10.70±4.40
R_{32}^{21}	2.20±0.30	2.10±0.30	2.00±0.20	2.00±0.20	1.90±0.20	1.80±0.20	1.80±0.20	1.90±0.20	2.30±0.30
R_{32}^{10}	0.40±0.10	1.10±0.10	0.90±0.10	0.90±0.10	1.10±0.10	0.90±0.10	1.10±0.10	1.00±0.10	1.10±0.20
R_{21}^{10}	0.18±0.03	0.50±0.06	0.46±0.05	0.44±0.04	0.55±0.05	0.52±0.05	0.62±0.08	0.54±0.07	0.48±0.07
R_{65}^{32}/R_{L4}	1.1±0.3	1.4±0.3	1.2±0.2	1.3±0.2	1.0	1.2±0.2	1.4±0.2	2.3±0.5	6.7±2.8
R_{65}^{21}/R_{L4}	1.2±0.3	1.5±0.3	1.3±0.2	1.4±0.2	1.0	1.1±0.2	1.3±0.2	2.2±0.4	8.0±3.4
R_{65}^{10}/R_{L4}	0.4±0.1	1.4±0.3	1.1±0.2	1.1±0.2	1.0	1.1±0.2	1.4±0.2	2.2±0.4	7.0±3.0
R_{32}^{21}/R_{L4}	1.1±0.2	1.1±0.2	1.0±0.1	1.0±0.1	1.0	0.9±0.1	0.9±0.1	1.0±0.2	1.2±0.2
R_{32}^{10}/R_{L4}	0.4±0.1	1.0±0.2	0.9±0.1	0.8±0.1	1.0	0.9±0.1	1.0±0.2	0.9±0.1	1.0±0.2
R_{21}^{10}/R_{L4}	0.3±0.1	0.9±0.1	0.8±0.1	0.8±0.1	1.0	0.9±0.1	1.1±0.2	1.0±0.2	0.9±0.2

(1-10) *First six rows:* Brightness temperature ratios between the different ^{12}CO transitions derived from the sum of all line peaks (Table 2). We converted all ^{12}CO integrated peak intensities from Jansky to Kelvin. *Rows seven to twelve:* Brightness temperature ratios with respect to peak L4, respectively.

profiles with multiple Gaussian components and given the high inclination of the disk in NGC 253, it is very likely that each of these peaks is an ensemble of GMCs at different velocities and merged along the line-of-sight. Based on recent ALMA observations of multiple lines in the 3 mm band, Leroy et al. (2015) find in total 10 different cloud components in their data, as based on dense gas tracers such as HCN and HCO, which appear to be fitted as well with up to three Gaussian components similar to our work. Their main components along the disk are in good agreement with those used in this study.

As a note, given the complexity of the peaks, we tried to run a clump finder program on our data cubes (e.g., GAUSSCLUMP from Stutzki & Guesten 1990), but we did not manage to obtain meaningful results due to the added complexity of an (almost) edge-on galaxy for the dynamics as well as the lack of angular resolution. Too many clumps are still merged together in space *and* velocity so that a clear separation and identification of GMCs remains very difficult at this point.

3.2.2. Line ratios

We calculated the brightness temperature ratios between $^{12}\text{CO}(J=6-5)$, $^{12}\text{CO}(J=3-2)$, $^{12}\text{CO}(J=2-1)$ and $^{12}\text{CO}(J=1-0)$, using different methods, first converting the intensities from Jansky to Kelvin. Fig. 8 shows the ratios between the spectrally integrated intensity maps from Fig. 4, while Table 5 lists the ratios determined from the line profiles shown in Fig. 7. We plot the individual line SEDs for each component and Gaussian component in Fig. 9. We also compare the line intensities sampled in bins of $\sim 1''$ and 12 km s^{-1} in Fig. 10 by using a mask for the different regions (being roughly twice the synthesized beam size); for components L1 to L7 we plot the different velocities in different colors to explore a possible dependence on velocity.

Along the disk, the spectrally integrated ratios (Fig. 8) show values of: $R_{32/65}^{\text{CO}} \simeq 1-2$, $R_{21/65}^{\text{CO}} \simeq 2-3$, $R_{10/65}^{\text{CO}} \simeq 0.5-1.5$, $R_{21/32}^{\text{CO}} \simeq 1-1.5$, $R_{10/32}^{\text{CO}} \simeq 0.5-1.5$ and $R_{10/21}^{\text{CO}} \simeq 0.3-0.7$, the range of which is lower than the values determined di-

rectly from the line components (Table 5). As Fig. 9 and Fig. 10 clearly indicate, there are indeed differences between the three different line components for each peak that appear to be identical in the different line transitions. This highlights the fact that at each position we probably see an ensemble of different GMCs which likely exhibit slightly different excitation conditions (see also Table 6). However, the differences are not very large so probably all of these GMCs are exposed to the same major heating source, the starburst and its winds/shocks.

While we cannot identify any significant difference in the ratios between the peaks along the disk (see also Columns 3-9 in Table 5 & 6, as well as Fig. 9), the temperature ratios are significantly lower close to the eastern shell SB2 indicating much warmer (and/or denser) material there (similar to the continuum emission) and slightly higher ratios toward the western shell SB1 indicating less warm (or less dense) gas there (see Figs. 8, 9 and 10). This difference in gas excitation between the two shells is quite surprising if one assumes a similar nature/origin of the two. However, there are some indications that the two shells are probably caused by different mechanisms: SB2 is associated with winds from a stellar cluster while SB1 is associated with a supernova remnant¹¹. The energetic output of a supernova is probably quite different from the stellar winds from star-formation/star-bursts in a stellar cluster so that a different feedback to the surrounding molecular gas is to be expected (see also Section 3.2.4). Another explanation could be that these shells are at different evolutionary stages, although they appear to exhibit a similar extent and expansion velocities (see Sakamoto et al. 2006; Bolatto et al. 2013) if one believes that SB1 is an expanding superbubble. As Sakamoto et al. (2011) expressed doubts about SB1 being a superbubble as opposed to SB2, SB1 might have a much different origin hence naturally explaining the different ratios and subsequently

¹¹ Although one single supernova remnant is probably not enough to create SB1 alone.

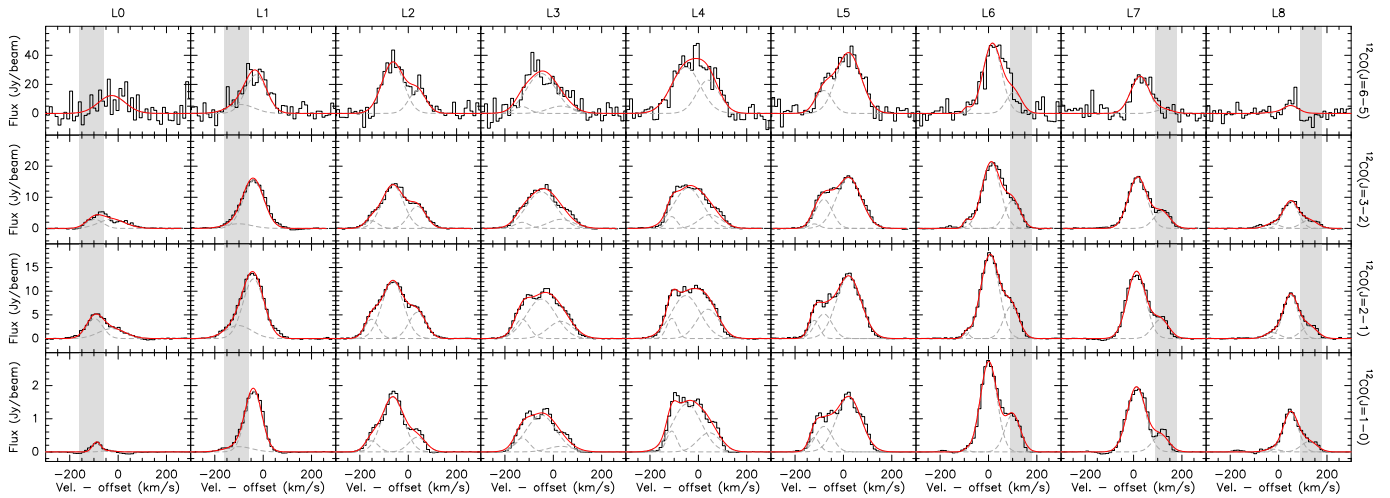


FIG. 7.— Line spectra for the different line peaks for each ^{12}CO transition. Each row corresponds to one transition (see labelling on the right) and each column to the different line peaks L0 to L8 (see labelling on the top). A Gaussian fit with up to three components has been applied to all spectra, shown as solid red (*sum*) and dashed grey curves (*individual components*). We fixed the velocities and FWHM during the fit to ensure that we fit the same components in all four transitions. The results of these fits are given in Table 2 and 4. The grey shaded areas approximately mark the velocity ranges for the eastern (around L0) and western shell (around L8 and close to L6/L7) in the wings of the line profiles.

different excitation conditions in these two regions.

However, we have to apply some caution in interpreting these ratios as we do not have exactly the same uv-coverages in the different ^{12}CO transitions, with $^{12}\text{CO}(J=6-5)$ probably being the least well sampled and the least sensitive. We already discussed the effect of spatial filtering flux in a previous section and found that resolution effects are possibly minor along the disk but could be more important in the region of the shells. Therefore, we think that the ratios along the disk are likely very representative while for the shells we probably need more sensitive observations of a larger field with better uv coverage, as is becoming possible with ALMA.

3.2.3. LVG Analysis

We conducted an LVG analysis with the RADEX code (see van der Tak et al. 2007) applying a reduced χ^2 minimization method to fit the basic excitation conditions of the molecular gas in the western and eastern shells and the (averaged) disk. We first considered a one phase gas model, i.e., gas at one kinetic temperature, one H_2 density and one CO column density. We thereby varied the temperatures by $T_{\text{kin}}=10-400$ K, the densities by $n_{\text{H}_2}=10^3-10^8$ cm^{-3} and the column densities by $N_{\text{CO}}=10^{14}-10^{19}$ cm^{-2} for a line width of $dv=100$ km s^{-1} (see also Leroy et al. 2015) and a uniform sphere, linearly splitting up the parameter space in 41 “bins” with steps of 10 K for T_{kin} and 0.1 dex for n_{H_2} and N_{CO} . All reduced χ_{red}^2 results for which the modelled line ratios are within at least $\sim 1-1.5\sigma$ of the observed line ratios (i.e., $\chi_{\text{red}}^2 \leq 1.5$) were considered as acceptable solutions. With these criteria we could fit the western and eastern shell quite reasonably, while we did not find any solution for the disk that could reproduce the high $^{12}\text{CO}(J=6-5)$ -to- $^{12}\text{CO}(J=1-0)$ ratio. This is in agreement with previous findings on the CO line SED of NGC 253 by different groups based on single-dish and/or satellite (*Herschel*) observations (e.g., Rosenberg et al. 2014; Hailey-Dunsheath et al. 2008). One approach is to allow for a two phase gas model by assuming two different kinetic temperatures with a upper limit of

the “cold” component at around $T_{\text{kin,cold}}=150$ K and $T_{\text{kin,warm}} > T_{\text{kin,cold}}$. The range of solutions found for the excitation conditions in the three different regions of NGC 253 are shown in Fig. 11. The respective range in kinetic temperatures for the two component model (middle panel) for a given volume and column density as well as the kinetic temperatures and column densities for the one component models for a given density (upper and lower panel) are plotted in Fig. 12.

Disk: As mentioned just before, a one temperature phase model largely underestimates the $^{12}\text{CO}(J=6-5)$ emission similar to previous findings (e.g., Rosenberg et al. 2014; Hailey-Dunsheath et al. 2008). Our best fit model suggests a very cold gas component at around 10 K and a very warm one at around 340 K with H_2 gas densities for both of $n_{\text{H}_2}=10^3-10^4$ cm^{-3} and CO column densities of $N_{\text{CO}} \simeq 10^{18}$ cm^{-2} (see Fig. 12). However, as can be seen in Fig. 11 and is indicated by the mediocre χ^2 values in Fig. 12, we find a large range of excitation conditions with similarly “good” χ^2 values as the best-fit model, certainly due to the fact that four observed lines are not sufficient to constrain well the parameter space with four free variables. Furthermore, although the best-fit models fit reasonably well the observed data, the modeled line ratios are only within $1.5-2\sigma$ of the observed ones indicating that a two temperature phase gas model is still insufficient to reproduce the data and the assumption of equal gas and column densities of the two gas phases is too simplistic. However, leaving those as free parameters as well between the two gas phases enforces more observational constraints, i.e., more line transitions and different molecular tracers need to be observed which is out of the scope of this paper.

Rosenberg et al. (2014) indeed argue that they need a three-temperature phase gas model to explain their ^{12}CO ladder, of which the phase-1 low temperature component is heated through PDRs. The phase-2 and 3 components are more likely heated mechanically while heating through cosmic rays seems to be rather negligible based on their models (see next Section but also Paglione & Abrahams 2012). The mechanical heating

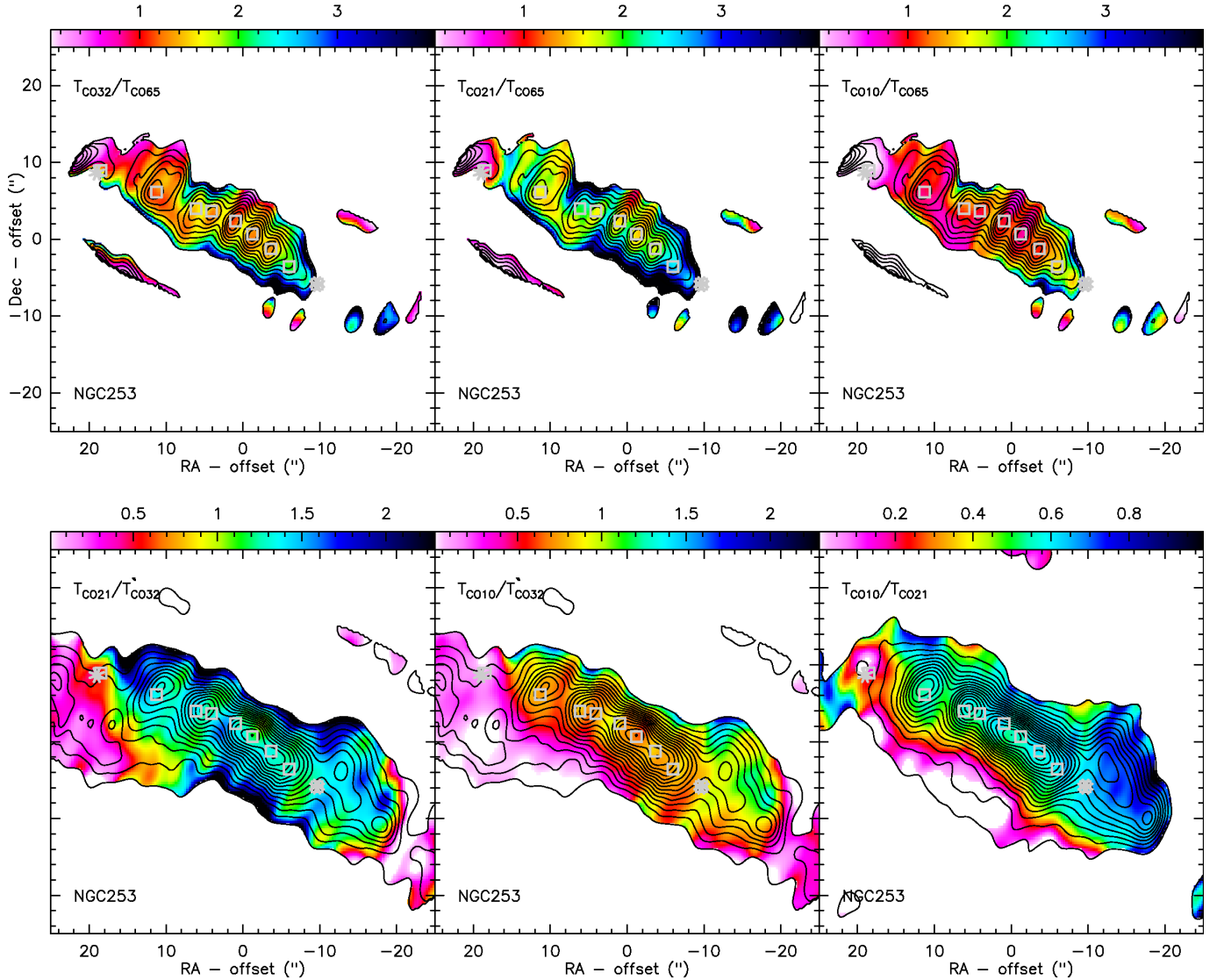


FIG. 8.— Temperature brightness ratios between the different integrated ^{12}CO line transitions. The grey symbols (squares and stars) are the same as in Fig. 4. Contours in the upper panels are those of the $^{12}\text{CO}(J=6-5)$ emission while those in the lower panels are from the $^{12}\text{CO}(J=1-0)$ line emission. Please note that we used a reversed color scale, i.e., for low ratios bright colors such as white, pink and red are used while high ratios are represented with darker colors such as blue and black. This was done to facilitate the connection between warm (and/or dense) molecular gas that is reflected here in low line ratios while cooler (and/or less dense) gas is shown by large line ratios.

through low-velocity shocks or turbulence is needed to produce the high temperatures throughout the surrounding clouds. PDRs affect only a thin layer of the surrounding molecular clouds and would potentially start to dissociate the CO molecules due to the strong UV-radiation fields (see also: Rosenberg et al. 2014; Goicoechea et al. 2013; Kaufmann & Neufeld 1996).

Western Shell (L8): Our best-fit solutions suggest for the western shell two main scenarios due to the $T_{\text{kin}}-n_{\text{H}_2}$ degeneracy of ^{12}CO in the excitation: either the molecular gas is at 1.) rather high kinetic temperatures around 300 K but low H_2 gas densities around $\sim 10^3 \text{ cm}^{-3}$, or 2.) at lower kinetic temperatures around 60 K but high H_2 gas densities around $\sim 5 \times 10^3 \text{ cm}^{-3}$ (see Fig. 11 and Fig. 12). Only in the low- T_{kin} /high- $n(\text{H}_2)$ case, the CO column density can be well constrained and show values of about $\sim 10^8 \text{ cm}^{-2}$, similar to the disk and the eastern shell (see Fig. 12), while the high- T_{kin} /low- $n(\text{H}_2)$ case leaves open almost the entire range of column densities sampled here. The HCN emission has been found

to be stronger (by a factor of ~ 3 in integrated fluxes) in the western shell compared to the eastern shell by Leroy et al. (2015). This is likely incompatible with the case in which the gas in the western shell is significantly less dense than in the eastern shell, favoring hence the low- T_{kin} /high- $n(\text{H}_2)$ case. The kinetic temperature in this case of 60 K is in between the cold ($T_{\text{kin}} \simeq 10 \text{ K}$) and hot ($T_{\text{kin}} \simeq 340 \text{ K}$) gas component found for the disk but much lower than found for the eastern shell (see next paragraph).

Eastern Shell (L0): The best fit solution for the eastern shell suggests higher kinetic temperatures ($T_{\text{kin}}=360 \text{ K}$) than the disk and the western shell but at similar H_2 densities ($n_{\text{H}_2} \simeq 5 \times 10^3 \text{ cm}^{-3}$) and CO column densities ($N_{\text{CO}} \simeq 10^{18} \text{ cm}^{-2}$). However, it seems that the best fit model slightly underestimates the $^{12}\text{CO}(J=2-1)$ emission as indicated by the lowest χ_{red}^2 of ~ 1.2 which means that not all modelled line ratios lie within 1σ of the observed ones. We also ran a two-temperature phase gas model for the eastern shell similar to the disk but we

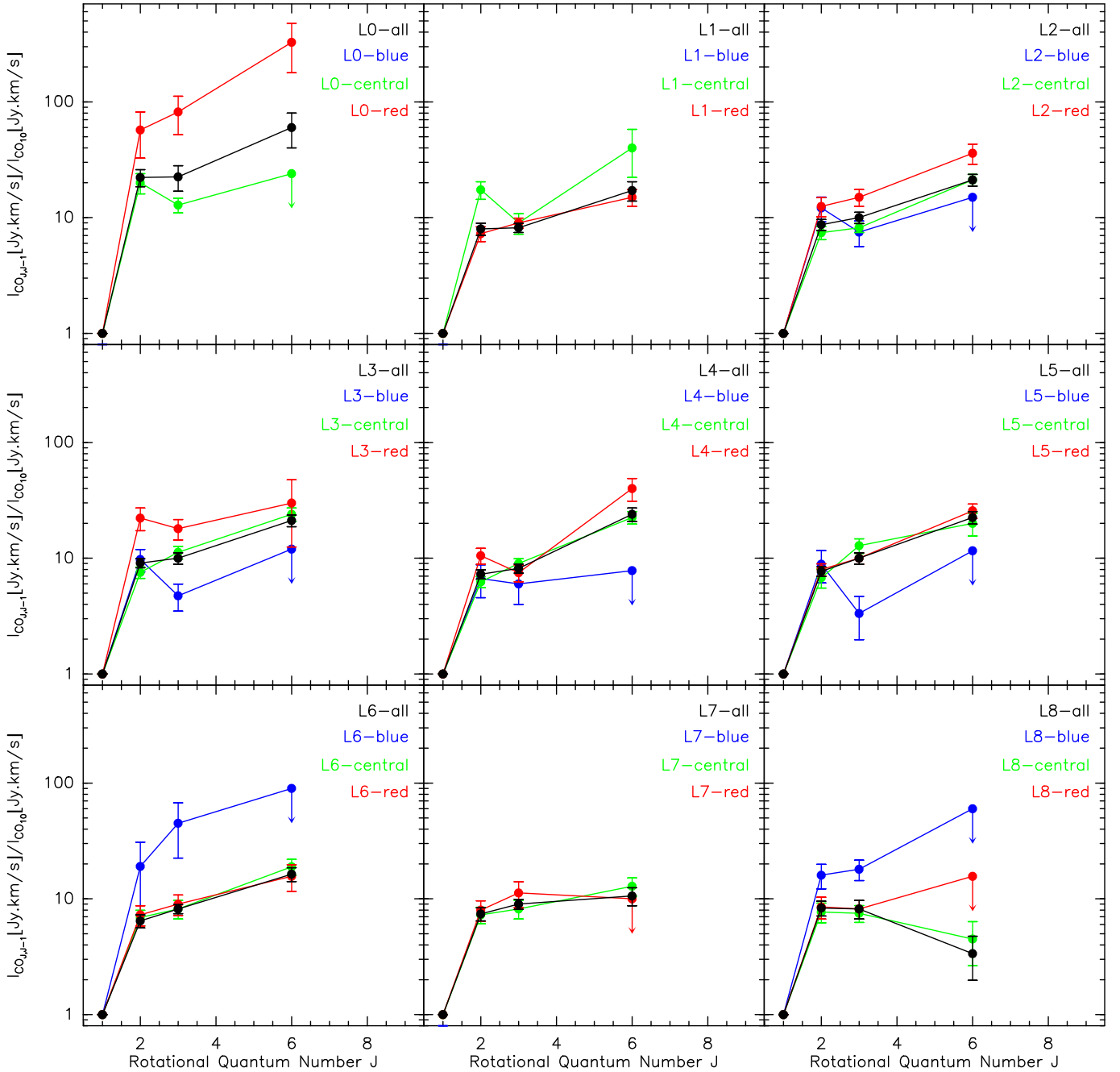


FIG. 9.— CO line SEDs for each position (L0-L9) and Gaussian component (in black (*sum*), blue (*blueshifted* velocities), green (*central* velocities) and red (*redshifted* velocities)). The line intensities, from which the line ratios were derived and plotted here, were not converted into temperature scale (K.km/s) first, as opposed to Tables 5 and 6, in order to stay consistent with CO line SEDs from other publications (e.g., Papadopoulos et al. 2010).

did not find a solution in which the $^{12}\text{CO}(J=2-1)$ emission was correctly reproduced. The best fit solutions of the two-temperature phase models largely resembled the one-temperature phase models so that we hence decided to keep the one-temperature phase model for the eastern shell for simplicity reasons. Either we are seeing (part of) the warm component from the disk only here or additional excitation mechanisms have to be considered.

3.2.4. Comparison to other multi-transition CO studies

Studies of spatially resolved, multi-transition (≥ 4) ^{12}CO emission in galaxies are still very rare. Most of them are conducted with single dish telescopes that provide sufficient angular resolution to resolve GMC

scales (≤ 50 -100pc) only in the most nearby galaxies or our own galaxy, if at all. We picked several ^{12}CO ladder studies in order to compare them to the results obtained on NGC 253 (Topal et al. 2014; Meijerink et al. 2013; Goicoechea et al. 2013; Danielson et al. 2011; van der Werf et al. 2010; Riechers et al. 2010; Carilli et al. 2010; Emprechtinger et al. 2009). The studied objects span from GMCs in the galactic center, over nearby starburst and/or AGN galaxies such as NGC6946, M82 and NGC 1068 to ULIRGs like Arp 220 and Mrk 231 and high-redshift galaxies.

Disk: Interestingly, all studies, i.e., for all (active)

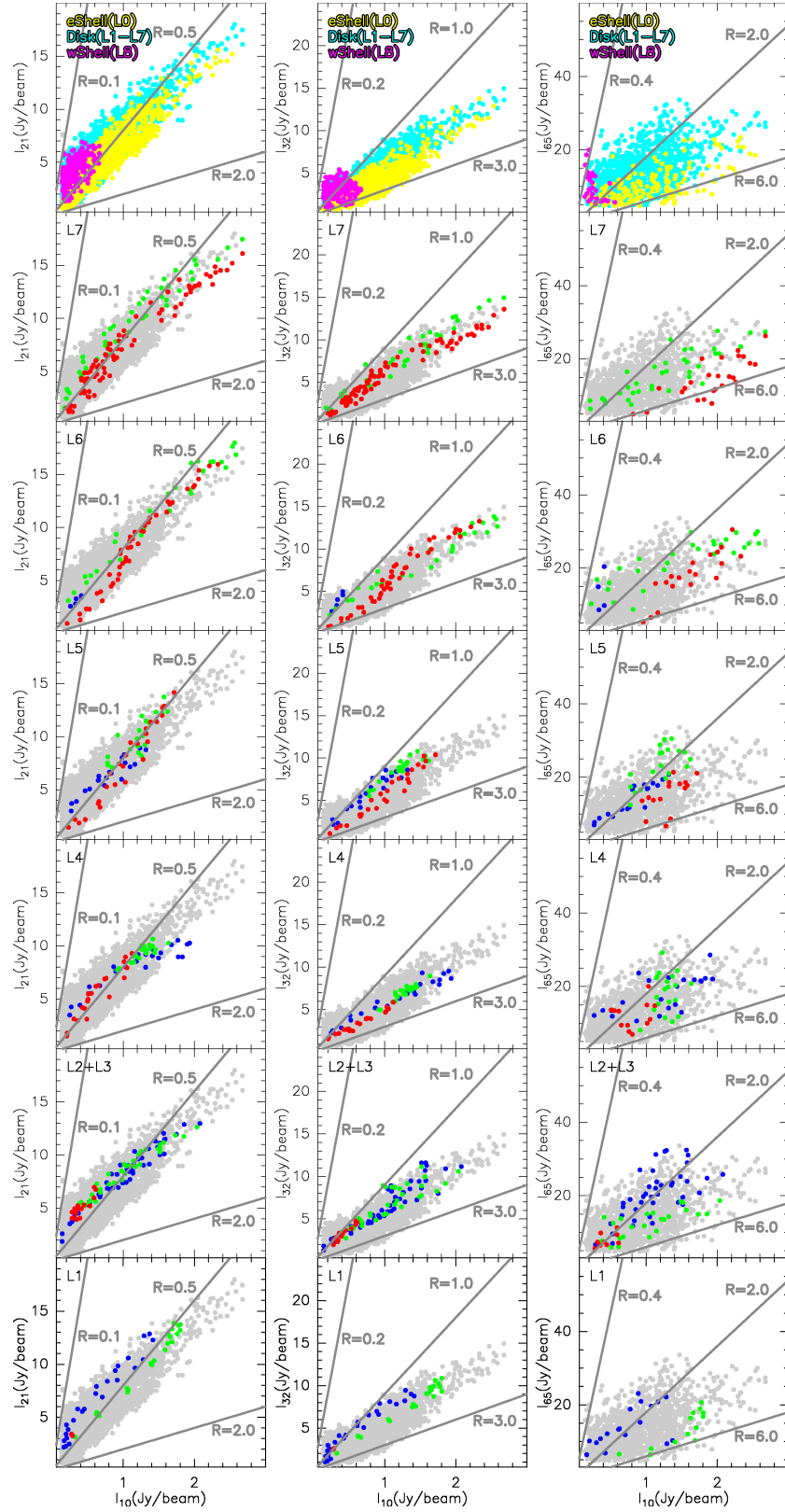


FIG. 10.— Comparison of ^{12}CO line fluxes for the different line transitions (left column: $^{12}\text{CO}(J=2-1)$ vs. $^{12}\text{CO}(J=1-0)$, middle column: $^{12}\text{CO}(J=3-2)$ vs. $^{12}\text{CO}(J=1-0)$, right column: $^{12}\text{CO}(J=6-5)$ vs. $^{12}\text{CO}(J=1-0)$) and regions in NGC 253 (L1-L8; from bottom to top) derived from data cubes with matching spatial and spectral resolution ($4''.2 \times 2''.1$ and 12 km s^{-1}); we defined a region of $\sim 8''$ (i.e. twice the synthesized beam) around each line peak defined in Fig. 4. We used a sampling spacing of ~ 4 pixels per beam. We only plot points that are above 3σ for $^{12}\text{CO}(J=6-5)$ and 10σ for the rest (due to the limited dynamical range). The red-, blue- and green-colored points represent the blueshifted ($< -40 \text{ km s}^{-1}$; in blue) and redshifted velocities ($> +40 \text{ km s}^{-1}$; in red) and around the systemic velocity of NGC 253 (i.e., from -40 km s^{-1} to $+40 \text{ km s}^{-1}$; in green), respectively. The grey data points are all data points, i.e. from all velocities and all regions. R represent the brightness temperature ratios and is defined as: $R = T_{\text{CO}10} / T_{\text{CO}J,J-1}$ for $J=6,3,2$. The solid lines are meant to guide the eyes for a given fixed ratio.

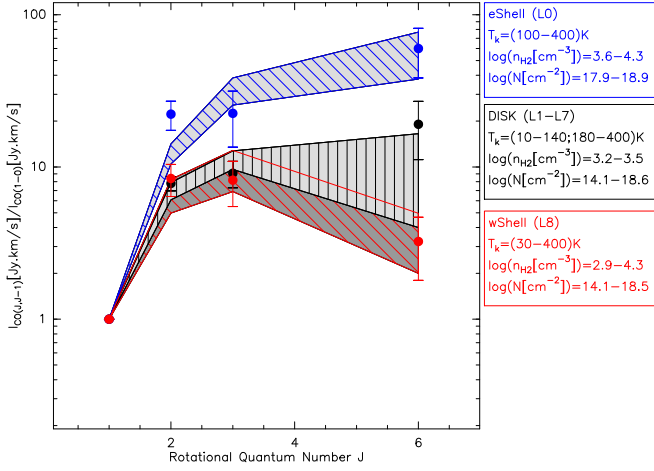


FIG. 11.— CO line SEDs for the eastern (*blue filled circles*) and western shell (*red filled circles*) and the central disk (*black filled circles*), summing up all Gaussian components. The *hashed grey areas* indicate the range of solutions with equally low χ^2_{red} -fits (i.e., solutions that are within $\sim 1-2\sigma$ of the observed values) from RADEX simulations to the line ratios (here derived from the intensities in Jy.km/s as opposed to Table 6, where they were derived from temperatures). The best fit solutions intervalls are given in the small colored boxes to the right.

environments in our vicinity up to the high-redshift universe, seem to need a multi-phase gas model (with at least a high and lower temperature gas component) to be able to reproduce the observed multi-transition CO emission (e.g., Topal et al. 2014; Goicoechea et al. 2013; Danielson et al. 2011; van der Werf et al. 2010; Riechers et al. 2010; Carilli et al. 2010; Emprechtinger et al. 2009; Weiß et al. 2005), similar to the central disk in NGC 253. Also, most of them find that besides photoelectric heating from UV radiation in PDRs also mechanical heating through low-velocity shocks have to be considered as almost equally dominant mechanism to heat the molecular gas (see also García-Burillo et al. 2014; Krips et al. 2011; García-Burillo et al. 2010). In all these regions, cosmic rays do not seem to contribute significantly to the heating of the warm molecular gas component, agreeing with the findings by Rosenberg et al. (2014) (see also Meijerink et al. 2011). On the other hand, NGC 253 has known supernova explosions at a rate of $< 0.2 \text{ yr}^{-1}$ (see Rampadarath et al. 2014; Paglione & Abrahams 2012) and, more importantly, a median cosmic ray ionisation rate of $\zeta_{\text{CR}} \simeq 6 \times 10^{-12} \text{ s}^{-1}$ (Paglione & Abrahams 2012). This is a factor of $\sim 100-1000$ higher than found in the vicinity of Sgr A* (Goto et al. 2008) and of the order of the X-ray(/cosmic ray) ionisation rates of $> 10^{-13} \text{ s}^{-1}$ found in the (U)LIRGs Arp 220 and NGC 4418 (González-Alfonso et al. 2013). Goicoechea et al. (2013) mention that already a cosmic ray ionisation rate of $\zeta_{\text{CR}} \simeq 10^{-14} \text{ s}^{-1}$ can heat the gas up to $\gg 10 \text{ K}$ and Paglione & Abrahams (2012) conclude that “cosmic ray penetration and heating is an important contributor to warm temperatures observed in starburst galaxies”. Although the simulations conducted by Rosenberg et al. (2014) favor a minor role of cosmic ray heating, it probably cannot be completely excluded at this point. Moreover, in the case of the ULIRG Mrk 231, van der Werf et al. (2010) find indications that, besides PDR heating, X-ray(/cosmic ray) heating

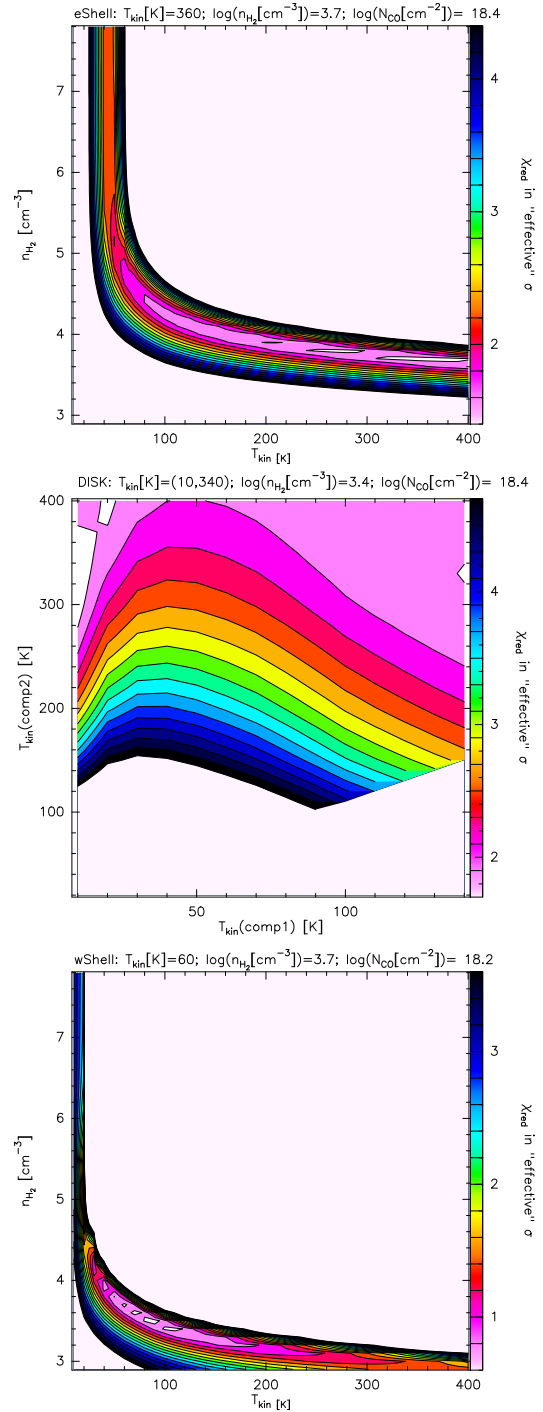


FIG. 12.— Best fit solutions with the lowest χ_{red} for the three different regions. For the one phase gas models of the western (wShell/L8) and eastern shells (eShell/L0; upper and lower panel) we plot the kinetic temperatures and CO column densities as function of χ_{red}^2 for a given H_2 density while for the two phase gas model we show the two kinetic temperatures for a given H_2 density and CO column density (given as $(T_{\text{kin}}(\text{comp1}), T_{\text{kin}}(\text{comp2}))$ above the middle panel with $T_{\text{kin}}(\text{comp1})$ for the “cold” and $T_{\text{kin}}(\text{comp2})$ for the warm gas phase). The reduced χ_{red} can be seen as effective σ s, meaning that a χ_{red} of 1 (2,...) represents modelled line ratios that are on average within 1σ (2σ ,...) of the respective observed line ratios. The solution with absolute lowest χ_{red} are given above each panel but note the range of possible solutions with equally low χ_{red} (these ranges are given in Fig. 11). The regions in pale pink have χ_{red} outside the range shown in the wedges and have been hence “blanked”.

is a significant contributor in order to explain their

two-temperature phase model of the multi-transition CO emission although they do not include shock models in their simulations. On the other hand, Rangwala et al. (2011) find in the case of Arp 220 that mechanical heating should be largely dominating over that by PDR, XDR and cosmic rays, at least for the warm molecular gas. This result might be logical as Arp 220 is a known major merger in an evolved merging stage so that mechanical heating should be quite significant. Although in a slightly earlier merger stage than Arp 220, Meijerink et al. (2013) argue for a (low velocity, C-type) shock domination of the gas heating in NGC 6240 as well, similar to Arp 220.

In contrast to NGC 1068, whose molecular gas in its central ~ 200 pc disk is most likely dominated by a combination of (low velocity) shocks and a giant XDR (e.g., Krips et al. 2011; García-Burillo et al. 2014; Viti et al. 2015), the line transition ratios in NGC 253 decrease (assuming $\text{CO}(J_{\text{upper}}-J_{\text{lower}})/\text{CO}(J=1-0)$; with $J_{\text{upper}} > 1$) while those for NGC 1068 increase. This is in good agreement with theoretical predictions of the ^{12}CO line ratios for XDRs and PDRs (Meijerink et al. 2006), even in the case of a strong cosmic ray ionisation field in addition to a PDR. Another interesting difference to note is that NGC 1068 indeed shows variations of its line ratios the closer one gets to the nucleus (central 50 pc or so) as revealed by recent ALMA Observations (see García-Burillo et al. 2014; Viti et al. 2015) while the disk (central 500 pc) appears to be dominated by the same heating source. Hence, a starburst influences its surrounding gas on a much larger scale than an AGN seems to do.

Shells: Based on the discussion of the heating mechanisms responsible for the CO ladder in diverse environments, one can draw some first conclusions on the dominant heating mechanisms for the two shells by simple comparison. As mentioned before, probably only mechanical energy from shocks or turbulent gas can heat up the bulk of molecular gas significantly above 50 K, while photo-electric (PDR) and/or cosmic ray heating dominates the cold to warm gas component. Our data quite clearly indicate that the eastern shell is much warmer than the disk and the western shell while being at similar gas and column densities. This could be hence an indication that shocks might play a much more dominant role in the eastern shell, associated with a compact stellar cluster, than in the PDR+shock dominated disk and the western shell which might be connected to a supernova remnant. It appears rather unlikely that a strong PDR (or cosmic rays) also has to be considered for the eastern shell which could explain the stronger emission in the higher-J transitions in it compared to the disk; the higher-J CO transitions are more dominantly excited than the lower-J CO transitions.

Our data suggest that the western shell is much colder than the eastern shell and the hot gas component of the disk but is still warmer than the cold gas component of the disk. One conclusion, although certainly quite speculative at this point, is that the cosmic rays from the supernova remnant dominate the gas excitation in the western shell and that the (low-velocity) shocks, if they

exist, from the SN explosion have not yet or only very inefficiently heated the gas to the same high temperatures as found in the (warm component of the) disk or the eastern shell. However, given the similar extent of both shells, it is not intuitive why shocks play such a minor role in the western shell compared to the eastern shell and the disk. Also, while it is true that SN have been identified through radio observations in the western shell, the lack of radio detections in the eastern shell does not exclude SN in it. Further observations of either ^{12}CO or other shock and cosmic ray tracers have to be conducted to unveil the heating mechanisms in these shells at a sufficient confidence level.

4. SUMMARY

We presented new interferometric observations of the extended $^{12}\text{CO}(J=6-5)$ line and 686 GHz continuum emission in NGC 253 carried out as a five point mosaic with the SMA. These data were then compared to three lower-J ^{12}CO transitions ($J=1-0$, $J=2-1$, $J=3-2$) and continuum emission at lower frequencies at similar angular resolution of $\sim 4''$ observed with ALMA and the SMA.

Five of the eight ^{12}CO line peaks find counterparts in the mm and submm continuum emission underlying the thermal nature of the continuum emission from dust as suggested by the spectral index of 3 determined from the different frequencies. The continuum emission at the lowest frequency of 115 GHz appears to exhibit already a significant contribution from non-thermal synchrotron and thermal free-free processes (between 15-80%) as supported by the spectral indices derived at cm wavelengths. We derive dust temperatures of ~ 10 -25 K for the different continuum peaks in the disk with low opacities of ~ 0.2 at 686 GHz. However, we also find indications for a hotter dust component at least in the inner disk of NGC 253 with dust temperatures exceeding 60 K and at much larger opacities of around 4 at 686 GHz. The latter dust component approaches the values found for ULIRGs such as Arp 220. We estimate a total dust mass of a few $10^6 M_{\odot}$ for the entire disk, splitting up into $\sim 10^4$ - $10^5 M_{\odot}$ for the GMCs at the individual continuum peaks. Based on the gas masses of each of the peaks, we find a gas-to-dust mass ratio of the order of ~ 100 -1000.

The $^{12}\text{CO}(J=6-5)$ emission follows nicely the distribution of the molecular gas seen in the lower-J transitions with roughly eight peaks along the disk. Only few $^{12}\text{CO}(J=6-5)$ emission is detected close to the two shells emerging from the edges of the central disk. While the ^{12}CO line transition ratios do not vary significantly along the disk, the two shells show quite different ratios not only compared to the disk but also to each other. The line ratios found along the disk seem to necessitate a two-phase gas model in agreement with previous studies on NGC 253 as well as multiple- ^{12}CO observations on other active galaxies. This two-phase gas model is mainly based on two temperatures, a cool gas component at around $T_{\text{kin}}=10$ K and hot gas component at around $T_{\text{kin}}=300$ K. Following a similar argumentation to previous publications, the lower temperature gas is probably dominated by the PDR while the higher temperature gas is a consequence of the shocks found throughout the disk (see also Rosenberg et al. 2012, 2014). However, a possible contribution from cosmic rays, given

the high cosmic ray ionisation rate within the disk, cannot be completely excluded for either temperature phase at this point although some simulations indicate only a minor role of cosmic ray heating (e.g., Rosenberg et al. 2014). While the eastern shell exhibits even warmer gas ($T_{\text{kin}} > 300$ K) with respect to the hot gas ($T_{\text{kin}} \simeq 300$ K) component of the disk, the western shell contains gas much cooler ($T_{\text{kin}} \simeq 60$ K) than the eastern shell but somewhere in between the two temperature gas components of the disk ($T_{\text{kin}}^{\text{cold}} \simeq 10$ K and $T_{\text{kin}}^{\text{hot}} \simeq 300$ K); the gas densities ($n(\text{H}_2) \simeq 5 \times 10^3 \text{ cm}^{-3}$) and column densities ($N(\text{CO}) \simeq 10^{18} \text{ cm}^{-2}$) are very similar between the two shells and the disk. This reflects either a different evolutionary stage of the shells, an additional, different or more efficient heating mechanism in the eastern shell, a very different nature of these two structures, or a combination thereof. However, follow-up observations are mandatory to put our findings for the shells onto a more solid basis.

The Submillimeter Array is a joint project between the Smithsonian Astrophysical Observatory and the Academia Sinica Institute of Astronomy and Astrophysics and is funded by the Smithsonian Institution and the Academia Sinica. This paper makes use of the following ALMA data: ADS/JAO.ALMA#2011.0.00172.S. ALMA is a partnership of ESO (representing its member states), NSF (USA) and NINS (Japan), together with NRC (Canada) and NSC and ASIAA (Taiwan), in cooperation with the Republic of Chile. The Joint ALMA Observatory is operated by ESO, AUI/NRAO and NAOJ. K.S. was supported by the grant NSC 102-2119-M-001-011-MY3. The National Radio Astronomy Observatory is a facility of the National Science Foundation operated under cooperative agreement by Associated Universities, Inc. We thank the anonymous referee for the thorough and constructive comments.

Facilities: SMA,ALMA.

REFERENCES

- Aladro, R., Martín, S., Martín-Pintado, J., Mauersberger, R., Henkel, C., Ocaña Flaquer, B. & Amo-Baladrón, M. A., 2011, *A&A*, 535, 84
- Bayet, E., Gerin, M., Phillips, T. G. & Contursi, A., 2004, *A&A*, 427, 45
- Bendo, G. J.; Beswick, R. J.; D’Cruze, M. J.; Dickinson, C.; Fuller, G. A.; Muxlow, T. W. B., 2015, *MNRAS*, 450, 80
- Beuther, H., Zhang, Q., Reid, M. J., et al, 2006, *ApJ*, 636, 323
- Bolatto, A., et al., *Nature*, 499, 450
- Bradford, C. M., Nikola, T., Stacey, G. J., Bolatto, A. D., Jackson, J. M., Savage, M. L., Davidson, J. A. & Higdon, S. J., 2003, *ApJ*, 586, 891
- Carilli, C. L., et al., 2010, *ApJ*, 714, 1407
- Carilli, C. L., Kohno, K., Kawabe, R., Ohta, K., Henkel, C., Menten, K. M., Yun, M. S., et al., 2002, *AJ*, 123, 1838
- Danielson, A.L.R., et al., 2011, *MNRAS*, 410, 1687
- Dayal, P.; Hirashita, H.; Ferrara, A., 2010, *MNRAS*, 403, 620
- Draine, B. T.; Lee, H. M., 1984, *ApJ*, 285, 89D
- Emprechtinger, M., et al., 2009, *A&A*, 496, 731
- Fabbiano, G. & Trinchieri, G., 1984, *ApJ*, 286, 491
- García-Burillo, S.; Martín-Pintado, J.; Fuente, A.; Neri, R., 2000, *A&A*, 355, 499
- García-Burillo, S.; Usero, A.; Fuente, A.; Martín-Pintado, J.; Boone, F.; Aalto, S.; Krips, M.; Neri, R.; Schinnerer, E.; Tacconi, L. J., 2010, *A&A*, 519, 2
- García-Burillo, S.; Combes, F.; Usero, A.; Aalto, S.; Krips, M.; Viti, S.; Alonso-Herrero, A.; et al. accepted for publication in *A&A*, eprint arXiv:1405.7706
- Goicoechea, J.R., et al., 2013, *ApJ* 769, L13
- González-Alfonso, E., et al., 2013, *A&A*, 550, 25
- Goto, M.; Usuda, T.; Nagata, T.; Geballe, T. R.; McCall, B. J.; Indriolo, N.; Suto, H.; Henning, T.; Morong, C. P.; Oka, T., 2008, *ApJ*, 688, 306
- Güsten, R., Philipp, S. D., Wei, A. & Klein, B., 2006, *A&AL*, 454, 115
- Hailey-Dunsheath, S.; Nikola, T.; Stacey, G. J.; Oberst, T. E.; Parshley, S. C.; Bradford, C. M.; Ade, P. A. R.; Tucker, C. E., 2008, *ApJ*, 689, L109
- Heckman, T. M., Armus, L. & Miley, G.K., 1990, *ApJS*, 74, 833
- Heesen, V.; Beck, R.; Krause, M.; Dettmar, R.-J., 2011, *A&A*, 535, 79
- Hirashita, H.; Ferrara, A.; Dayal, P.; Ouchi, M., 2014, *MNRAS*, 443, 1704
- Houghton, S.; Whiteoak, J. B.; Koribalski, B.; Booth, R.; Wiklind, T.; Wiełebinski, R., 1997, *A&A*, 325, 923
- Kaufmann, M.J., Neufeld, D.A., 1996, *ApJ*, 456, 611
- Knudsen, K. K., Walter, F., Weiss, A., Bolatto, A., Riechers, D. A. & Menten, K., 2007, *ApJ*, 666, 156
- Koribalski, B.S.; et al., 2004, *AJ*, 128, 16
- Krips, M., Martín, S., Eckart, A., et al., 2011, *ApJ*, 736, 37
- Krips, M., Neri, R., García-Burillo, S., et al., 2008, *ApJ*, 677, 262
- Leroy, A. K., et al., 2015, *ApJ*, 801, 25
- Martín, S., Martín-Pintado, J. & Viti, S., 2009, *ApJ*, 706, 1323
- Martín, S., Mauersberger, R., Martín-Pintado, J., Henkel, C. & García-Burillo, S., 2006, *ApJS*, 164, 450
- Matsushita, S., Iono, D., Petitpas, G.R., et al., 2009, *ApJ*, 693, 56
- Meier, D., S.; 2015, *ApJ*, 801, 63
- Meijerink, R., et al., 2013, *ApJ*, 762, L16
- Meijerink, R., Spaans, M., Loenen, A.F., & van der Werf, P.P., 2011, *A&A*, 525, 119
- Meijerink, R., Spaans, M., & Israel, F.P., 2006, *ApJ*, 650, L103
- Minh, Y. C., Muller, S., Liu, S.-Y. & Yoon, T. S., 2007, *ApJ*, 661, L135
- Mouhcine, M.; Ferguson, H. C.; Rich, R. M.; Brown, T. M.; Smith, T. E., 2005, *ApJ*, 633, 810
- Müller-Sánchez, F.; González-Martín, O.; Fernández-Ontiveros, J. A.; Acosta-Pulido, J. A.; Prieto, M. A., 2010, *ApJ*, 716, 1166
- Nakashima, J.-I.; Fong, D.; Hasegawa, T.; et al., 2007, *AJ*, 134, 2035
- Ott, J.; Weiss, A.; Henkel, C.; Walter, F., 2005, *ApJ*, 629, 767
- Papadopoulos, P.P.; van der Werf, P.; Isaak, K.; Xilouris, E. M., 2010, *ApJ* 715, 775
- Papadopoulos, Padelis P.; Isaak, Kate G.; van der Werf, Paul P., 2007, *ApJ* 668, 815
- Paglionie, T.A.D., & Abrahams, R.D., 2012, *ApJ*, 755, 106
- Peel, M. W.; Dickinson, C.; Davies, R. D.; Clements, D. L.; Beswick, R. J., 2011, *MNRAS*, 416, 99
- Qi, C.; Wilner, D.J.; Calvet, N.; 2006, *ApJ*, 636, L157
- Rampadarath, H.; Morgan, J.S.; Lenc, E., Tingay, S.J., 2014, *AJ*, 147, 5
- Rangwala, N. et al., 2011, *ApJ*, 743, 94
- Rekola, R.; Richer, M. G.; McCall, M.L.; Valtonen, M. J.; Kotilainen, J. K.; Flynn, C., 2005, *MNRAS*, 361, 330
- Rmy-Ruyer, A.; et al., 2014, *A&A*, 563, 31
- Riechers, D., et al., 2010, *ApJ*, 729, L131
- Rolfs, R.; Schilke, P.; Zhang, Q.; Zapata, L., 2011, *A&A*, 536, 33
- Rosenberg, M.J.F., van der Werf, P.P., Israel, F.P., 2012, *A&A*, 550, 12
- Rosenberg, M. J. F.; Kazandjian, M. V.; van der Werf, P. P.; Israel, F. P.; Meijerink, R.; Weiß, A.; Requena-Torres, M. A.; Güsten, R., 2014, *A&A*, 564, 126
- Sakamoto, K.; Mao, R.-Q.; Matsushita, S.; Peck, A.B.; Sawada, T.; Wiedner, M. C., 2011, *ApJ*, 735, 19
- Sakamoto, K.; Ho, P. T. P.; Iono, D., et al, 2006, *ApJ*, 636, 685
- Scoville, N., et al., 2015, *ApJ*, 800, 70
- Sliwa, K.; Wilson, Ch. D.; Krips, M.; Petitpas, G. R.; Iono, D.; Juvela, M.; Matsushita, S.; Peck, A.; Yun, M., accepted for publication in *ApJ*, arXiv:1309.1144
- Storey, P. J.; Hummer, D. G., 1995, *MNRAS*, 272, 41S
- Stutzki, J.; & Guesten, R., 1990, *ApJ*, 356, 513
- Telesco, C. M.; Harper, D. A., 1980, *ApJ*, 235, 392
- Topal, S.; Bayet, E.; Bureau, M.; Davis, T. A.; Walsh, W., 2014, *MNRAS*, 437, 1434
- Ulvestad, J.S., & Antonucci, R.R.J., *ApJ*, 488, 621

- van der Tak, F. F. S., Black, J. H., Schöier, F. L., Jansen, D. J., & van Dishoeck, E. F. 2007, *A&A*, 468, 627
- van der Werf et al., 2010, *A&A*, 518, L42
- Viti, S., et al., 2014, *A&A*, 570, 28
- Weiß, A.; Walter, F.; Scoville, N. Z., 2005, *A&A*, 438, 533
- Wilson, C.D.; Rangwala, N.; Glenn, J.; Maloney, P.R.; Spinniglio, L., & Pereira-Santaella, M.; 2014, *ApJ*, 789, L36
- Xu, C. K.; Cao, C.; Lu, N.; Gao, Y.; van der Werf, P.; Evans, A. S.; Mazzarella, J. M.; et al. 2014, *ApJ*, 787, 48
- Xu, C. K.; et al., 2015, *ApJ*, 799, 11
- Zapata, L. A.; Loinard, L.; Rodríguez, L. F.; Hernández-Hernández, V.; Takahashi, S.; Trejo, A.; Parise, B., 2013, *ApJ*, 764, L14
- Zubko, V.; Dwek, E.; Arendt, R.G., 2004, *ApJS*, 152, 211
- Zubko, V. G.; Mennella, V.; Colangeli, L.; Bussoletti, E., 1996, *MNRAS*, 282, 1321